iScience

CellPress
OPEN ACCESS

Article

IRP1 mediated ferroptosis reverses temozolomide resistance in glioblastoma via affecting LCN2/FPN1 signaling axis depended on NFKB2

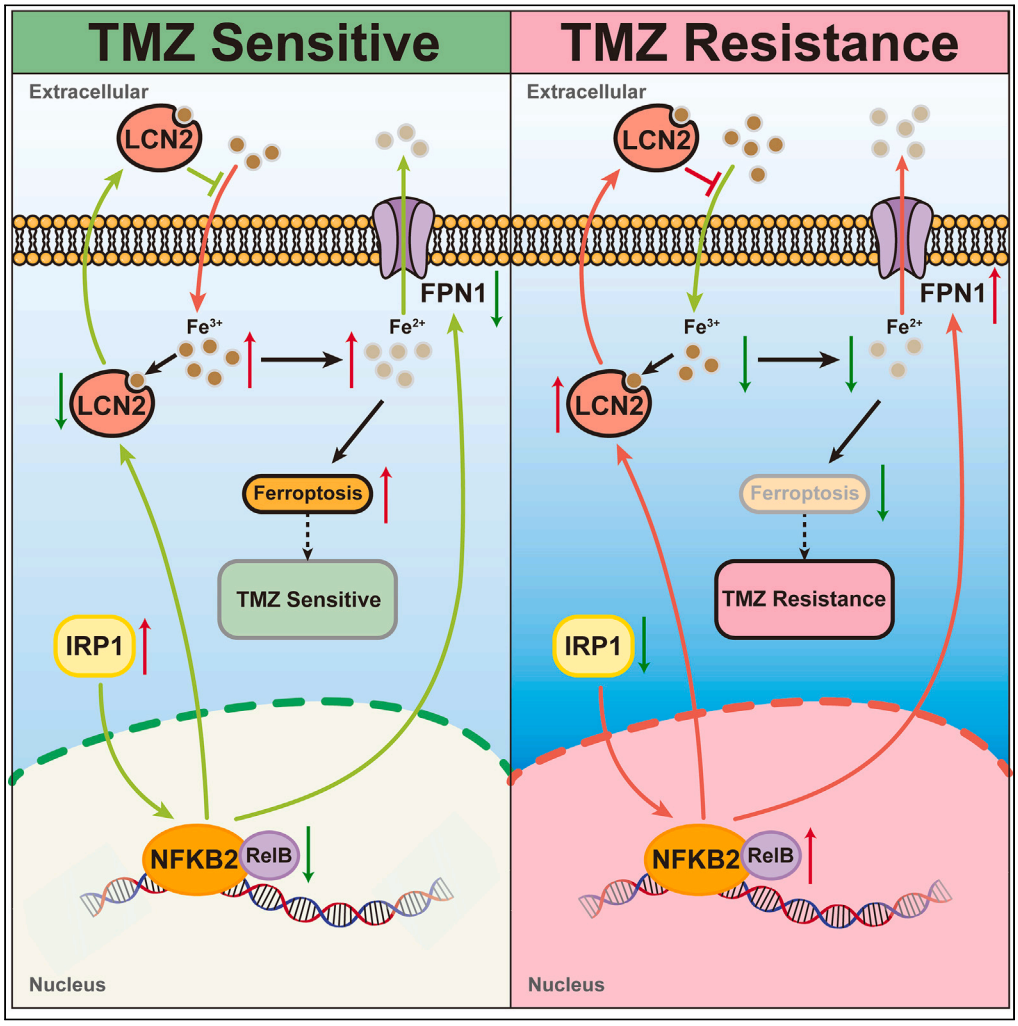

Yufei Lan, Tao Yang, Qu Yue, ..., Tianci Zeng, Boyang Liu, Hongbo Guo

lby19881118@163.com (B.L.)
guohongbo911@126.com (H.G.)

Highlights

IRP1 can act as a tumor suppressor to predict clinical prognosis of GBM

IRP1 can confer TMZ resistance to GBM cells by attenuating ferroptosis

The IRP1-NFKB2-LCN2/FPN1 signaling axis is critical for regulating TMZ resistance

The sensitivity of GBM to TMZ can be increased via upregulating IRP1 expression

Lan et al., iScience 26, 107377
August 18, 2023
https://doi.org/10.1016/j.isci.2023.107377

iScience

CellPress
OPEN ACCESS

Article

IRP1 mediated ferroptosis reverses temozolomide resistance in glioblastoma via affecting LCN2/FPN1 signaling axis depended on NFKB2

Yufei Lan,[1] Tao Yang,[1] Qu Yue,[1] Zhao Wang,[1] Xiangyang Zhong,[1] Xin Luo,[1] Boming Zuo,[1] Manqing Zhang,[1] Tianci Zeng,[1] Boyang Liu,[1,2,*] and Hongbo Guo[1,2,3,*]

SUMMARY

The prognosis of glioblastoma (GBM) patients is poor, and temozolomide (TMZ) resistance has become an important obstacle to its treatment effect. A growing number of researches have revealed the special characteristics of iron metabolism in GBM chemosensitivity. Iron regulatory protein 1 (IRP1) is an important protein for maintaining intracellular iron homeostasis. IRP1 has been indicated to have additional vital roles beyond its conventional metabolic activity, but the underlying mechanisms and biological consequences remain elusive. Here, we unprecedentedly demonstrated that amplifying IRP1 signals can reverse TMZ resistance and suppress tumor growth *in vivo* via inhibiting NFKB2 in the noncanonical NF-κB signaling pathway. In addition, we identified that NFKB2 affected TMZ sensitivity of GBM by modulating the expression of LCN2 and FPN1. Taken together, this study established a role for the IRP1/NFKB2 pathway in regulating LCN2/FPN1 signaling axis among the progression of TMZ resistance, suggesting a potential innovative GBM therapeutic strategy.

INTRODUCTION

Glioma is the most common primary tumor in the brain, which is characterized by rapid malignant progress, insensitivity to radiotherapy and chemotherapy, high recurrence and mortality, and poor prognosis.[1,2] Gliomas have traditionally been classified into low-grade versus malignant, high-grade tumors on the basis of cellular density, nuclear atypia, mitotic index and presence of necrosis, defining pathological grades I through IV.[3] Among these, grade IV glioma, or glioblastoma multiforme (GBM), remains one of the deadliest cancers, with the 5-year survival rate less than 6%.[4–6] At present, the first-line orphan chemotherapy drug for clinical treatment of GBM is temozolomide (TMZ), but it is found that some patients are not sensitive to TMZ, and the sensitive patients can develop drug resistance after treatment, significantly limiting the clinical efficacy of TMZ.[7] Therefore, it is urgent to identify effective new targets for chemotherapy in GBM. GBM cells have altered the expression of many iron metabolism-related proteins and iron-related enzyme activities compared with normal cells.[8] These changes generally contribute to the relatively high availability of iron in GBM cells and promote the function of iron-dependent proteins involved in many physiological processes, such as tumorigenesis, progression, and metastasis.[9,10] Targeting iron-related proteins or increasing intracellular iron levels is considered a viable strategy for the treatment of cancer.[11] Understanding the molecular mechanisms involved in this process in GBM will help to exploit the application of ferroptosis for reversing the clinical TMZ resistance of glioma.

Ferroptosis is a new type of programmed cell death, which is driven by iron-dependent phospholipid peroxidation. The typical feature is the inactivation of the intracellular reducing system and excessive accumulation of reactive oxygen species (ROS), which leads to the rupture of the cell membrane. Under the electron microscope, the crista of mitochondria decreased or disappeared and the outer membrane thickened and ruptured. Although the physiological function of ferroptosis has not been clearly defined, the ability of ROS to accumulate in excess of glutathione (GSH) has been shown to induce ferroptosis.[12,13] The occurrence and execution of iron death mainly depend on the interaction of iron metabolism, lipid metabolism, and cysteine,[14] but the sensitivity of iron death is also regulated by some other key molecules and related mechanisms. Researches showed that iron-rich microenvironment is the main cause of cancer and maintaining tumor malignancy, which indicates the importance of iron death in malignant tumors.[15] Ferroptosis

[1]Department of Neurosurgery Center, The National Key Clinical Specialty, The Engineering Technology Research Center of Education Ministry of China on Diagnosis and Treatment of Cerebrovascular Disease, Guangdong Provincial Key Laboratory on Brain Function Repair and Regeneration, The Neurosurgery Institute of Guangdong Province, Zhujiang Hospital, Southern Medical University, Guangzhou 510282, China

[2]These authors contributed equally

[3]Lead contact

*Correspondence: lby19881118@163.com (B.L.), guohongbo911@126.com (H.G.)

https://doi.org/10.1016/j.isci.2023.107377

involves with many proteins and multiple pathways and, intriguingly, has been correlated with cancer therapy resistance, and inducing ferroptosis has been demonstrated to reverse drug resistance.[16] However, its role in the TMZ resistance of GBM and the specific mechanism is not fully clear, targeted trigger ferroptosis can collaborative treatment of malignant tumor death, enhance chemotherapy sensitivity, is expected to be a new strategy for tumor therapy.

In normal cells, intracellular iron homeostasis is tightly regulated at the level of uptake, storage, export, and even the microenvironment. Dysregulation of iron homeostasis leads to altered cell fate and promotes cancer.[17] Many types of cancer have alterations in iron metabolism that lead to elevated intracellular iron levels, which contribute to malignant cell growth and disease progression. Cells take up iron-transferrin through transferrin receptor-mediated endocytosis and store iron mainly in cytoplasmic ferritin. Two iron regulatory proteins (IRP1 and IRP2) act as cytoplasmic iron sensors. Iron regulatory protein 1 (IRP1, also known as ACO1), regulates the expression of ferritin and transferrin at the post-transcriptional level to maintain intracellular iron homeostasis.[18] In addition, IRP1 can also bind to iron-sulfur clusters to affect cellular iron homeostasis and regulate ferroptosis. However, IRP2 is principally thought to be regulated at the protein level via E3 ubiquitin ligase FBXL5-mediated degradation.[19] When cellular iron content is low, IRPs stabilize transferrin receptor mRNA, thereby increasing the number of transferrin receptors for iron uptake. Iron-deficient IRPs also inhibit translation of ferritin mRNA, resulting in a net release of iron from ferritin.[20] So far, there has been a particular paucity of research in the area of IRP1's role in the occurrence and development of tumors.

In the progression of GBM, many pathways play corresponding roles, especially NF-κB, Wnt, and PI3K/AKT/mTOR pathways.[21] Among the signaling pathways active in GBM, the nuclear factor-κB (NF-κB) response plays an important role in promoting tumor pathobiology and response to therapy, especially for the TMZ resistance.[22] Ferroportin 1 (FPN1, also known as solute carrier family 40 member 1, SLC40A1) is the only discovered mammalian iron efflux transporter in the plasma membrane and it mediates iron releases from cells. FPN1 deficiency results in intracellular iron overload and lipid peroxidation, thereby inducing ferroptosis.[23] The latest research showed that targeting FPN1 could induce ferroptosis in human glioblastoma cells,[24] which indicates the potential role of FPN1 in TMZ resistance. Lipocalin 2 (LCN2) is a secreted glycoprotein and may regulate iron homeostasis.[16] A recent study showed that overexpressed LCN2 was correlated with 5-fluorouracil resistance in colon cancer. Targeting LCN2 overcame 5-fluorouracil resistance by increasing intracellular iron levels, which in turn led to tumor cell ferroptosis.[25] Researchers also found that neoadjuvant chemotherapy treatment leads to LCN2 upregulation in residual human breast tumors, which correlates with worse overall survival.[26] FPN1 and LCN2 can transport ferrous iron and ferric iron out of cells respectively, resulting in the intracellular iron level changes to a certain extent.[27]

In this study, we seek to identify the specific function and mechanism of IRP1 in TMZ resistance. Unprecedentedly, we found that IRP1 showed low expression in TMZ resistant cells to maintain iron homeostasis in GBM cells, protect cancer cells from ferroptosis and reduce chemotherapy sensitivity. Furthermore, we uncovered that IRP1 mediated TMZ resistance by affecting NFKB2 expression level in the non-canonical NF-κB pathway, which in turn affected the downstream LCN2/FPN1. This knowledge will aid in the development of potential therapeutic strategies to ameliorate the decreased efficacy of GBM due to TMZ resistance.

RESULTS

Reduced IRP1 expression mediates resistance to ferroptosis in TMZ-resistant glioblastoma cells

We used parental cells and Temozolomide-resistant (TR) cells which have different sensitivities to TMZ to explore the molecular mechanisms underlying the different sensitivity of parental and resistant cells to ferroptosis (Figure S1A). The alteration of ferrous iron plays a key role in ferroptosis, and the level of ferrous iron can reflect the degree of ferroptosis upon erastin treatment (Figure S1B). Ferroptosis is characterized by lipid peroxidation, and the final product of lipid peroxidation is malondialdehyde (MDA).[13] Thus, we examined whether erastin could led to changes in MDA levels of parental and TR cells. MDA levels were significantly increased in parental cells compared to the control groups, showed that TR cells were less sensitive to ferroptosis (Figure S1C). In response to ferroptosis, there were corresponding changes in GSH and Glutathione oxidized (GSSG) levels, both of which results proved that the TR cells were less sensitive to ferroptosis compared with the parental group (Figures S1D and S1E). These results showed that TMZ-resistant cells were less sensitive to ferroptosis.

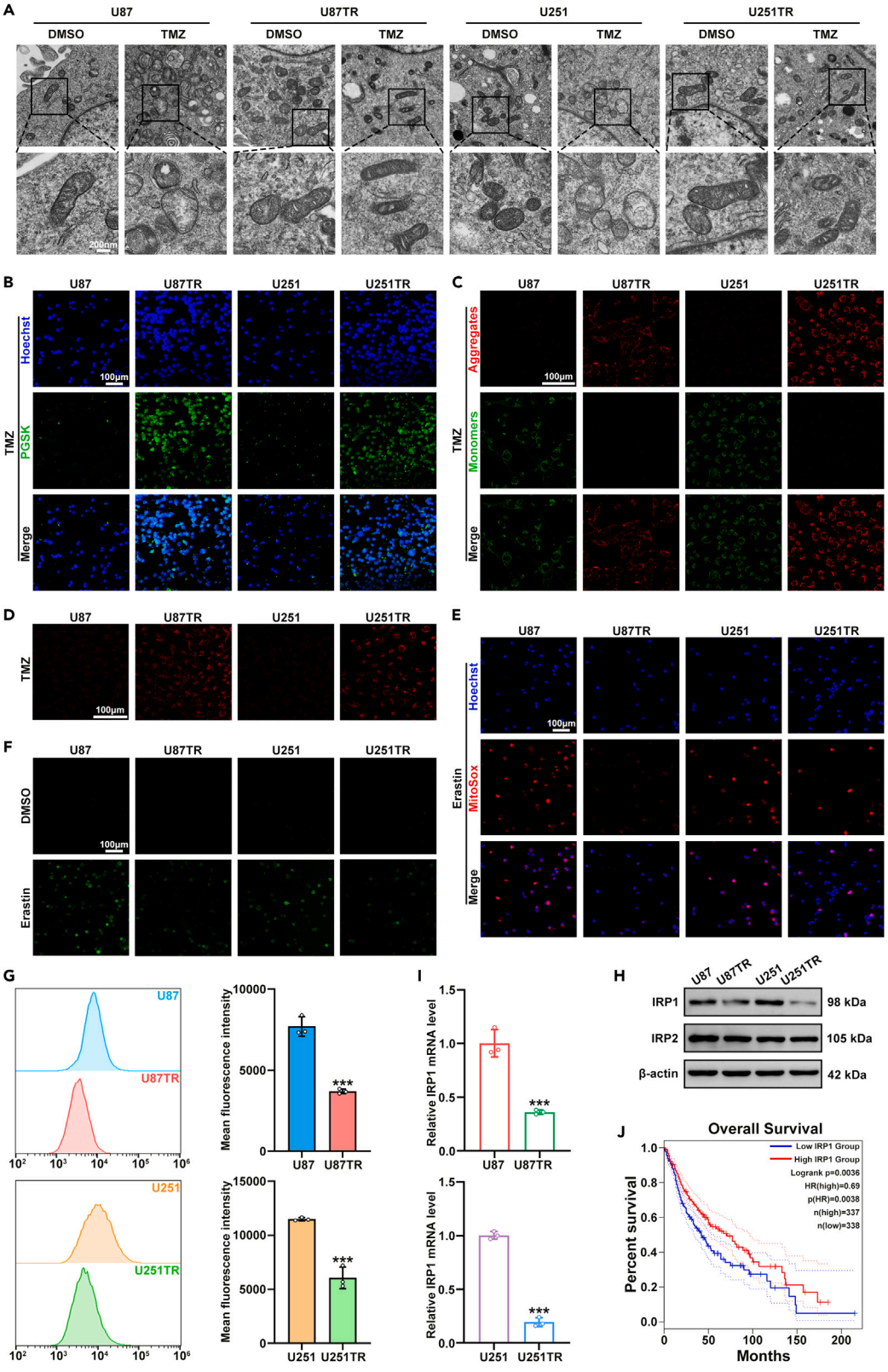
A
U87
U87TR
U251
U251TR
DMSO
TMZ
200nm
B
U87
U87TR
U251
U251TR
Hoechst
PGSK
Merge
TMZ
100μm
C
Aggregates
Monomers
D
E
MitoSox
Erastin
F
DMSO
G
U87
U87TR
U251
U251TR
Mean fluorescence intensity
***
H
IRP1
IRP2
β-actin
98 kDa
105 kDa
42 kDa
I
Relative IRP1 mRNA level
J
Overall Survival
Low IRP1 Group
High IRP1 Group
Logrank p=0.0036
HR(high)=0.69
p(HR)=0.0038
n(high)=337
n(low)=338
Percent survival
Months

Figure 1. Reduced IRP1 expression mediates resistance to ferroptosis in TMZ-resistant glioblastoma cells

(A) Images from transmission electron microscopy showing morphology of mitochondria in U87, U87TR, U251, U251TR cells after TMZ treatment for 24 h. Scale bar, 200 nm (down).

(B) Representative confocal images of U87, U87TR, U251 and U251TR cells stained with the PGSK (green) probe to assess intracellular iron levels. Scale bar, 100 μm.

(C) Representative confocal images of the cells stained with the JC-1 probe (Aggregates, red; Monomers, green) to assess mitochondrial membrane potential. Scale bar, 100 μm.

(D) Representative confocal images of U87, U87TR, U251 and U251TR cells stained with the TMRE (red) dye to assess mitochondrial membrane potential. Scale bar, 100 μm.

(E) Representative confocal images of the cells stained with the MitoSOX Red reagent (red) to assess mitochondrial ROS levels. Scale bar, 100 μm.

(F) Representative confocal images of the cells treated with erastin (10 μM) for 24 h stained with the DCF-DA (green) dye to assess cellular ROS. Scale bar, 100 μm.

(G) Lipid peroxidation level in parental and TR cells was influenced by erastin (10 μM) 24 h assessed by DCF-DA using flow cytometry immunolabelling.

(H) Western blot analysis of IRP1 and IRP2 protein levels in parental and TR cells.

(I) qRT-PCR to detect IRP1 mRNA levels in parental and TR cells.

(J) Kaplan–Meier survival analysis of patient overall survival data based on high versus low expression of IRP1 from the TCGA dataset.

In order to observe the difference of internal substructure changes between parental cells and TR cells upon TMZ treatment, we applied transmission electron microscopy to detect. The images showed that mitochondrial cristas were decreased or disappeared, mitochondrial outer membrane was thickening and the ruptures were more remarkable in parental cells than in drug-resistant cell lines after TMZ treatment (Figure 1A).

Since iron levels are the first to be affected during ferroptosis, the PGSK iron probe was used to detect the difference in intracellular iron levels between parental and TR cells after TMZ treatment. In cells undergoing ferroptosis, the green fluorescence of PGSK will be weakened, and as shown in confocal images, parental cells are more susceptible to ferroptosis after TMZ treatment (Figure 1B). It was also confirmed by the change of ferroptosis marker PTGS2 mRNA level (Figure S1F).

After TMZ treated, ferroptosis inhibitor, apoptosis inhibitor, and necrosis inhibitor were used respectively, and the results demonstrated that ferroptosis inhibitor reversed the TMZ-induced cell death significantly, proving that ferroptosis plays a vital role in TMZ-induced GBM cell death (Figure S1G).

Increased intracellular iron can induce ferroptosis, and a hallmark of ferroptosis is morphological changes in mitochondria. JC-1 dye aggregates at high concentrations and emits red fluorescence in normal mitochondria, while it presents as a low concentration of green fluorescent monomers under depolarization. Therefore, we applied the ratio of red to green fluorescence among the JC-1 dye in cells to demonstrate possible changes in mitochondrial membrane potential (Figure 1C). We clearly found that the decrease of mitochondrial membrane potential in parental cells compared with TR cells, and the results reflected the parental cells were more sensitivity to ferroptosis.

Mitochondria are the main energy source in cells and play important roles in processes of ferroptosis, and the mitochondrial membrane potential is a key indicator of its function and cell survival. The dissipation of mitochondrial membrane potential is established as an early indicator for ferroptosis. Therefore, we used TMRE (tetramethylrhodamine, ethyl ester), a cell membrane permeable cationic dye, to measure the changes in mitochondrial membrane potential upon TMZ treatment in parental or TR cells (Figure 1D). The results indicated that TR cells were less susceptible to ferroptosis.

Mitochondrial superoxide, a byproduct of oxidative phosphorylation, could be used to detect the degree of mitochondrial oxidative phosphorylation in producing ROS. MitoSOX Red is a live-cell permeant reagent and it can be rapidly and selectively targeted to the mitochondria. Once MitoSOX Red reagent enters into the mitochondria, it will be oxidized by superoxide and exhibits red fluorescence. Confocal images showed that parental cells were more prone to superoxide production after erastin treatment for 24 h, indicating that they were more sensitive to ferroptosis than TR cells (Figure 1E).

Intracellular ROS can oxidize non-fluorescent DCFH to generate fluorescent DCF, so the level of intracellular ROS can be known via detecting the fluorescence of DCF. Both the confocal images and flow cytometry results showed that parental cells could significantly increase the lipid peroxidation level as compared to TR cells (Figures 1F and 1G). The statistical result of the DCF-DA positive ratio was also shown on the right.

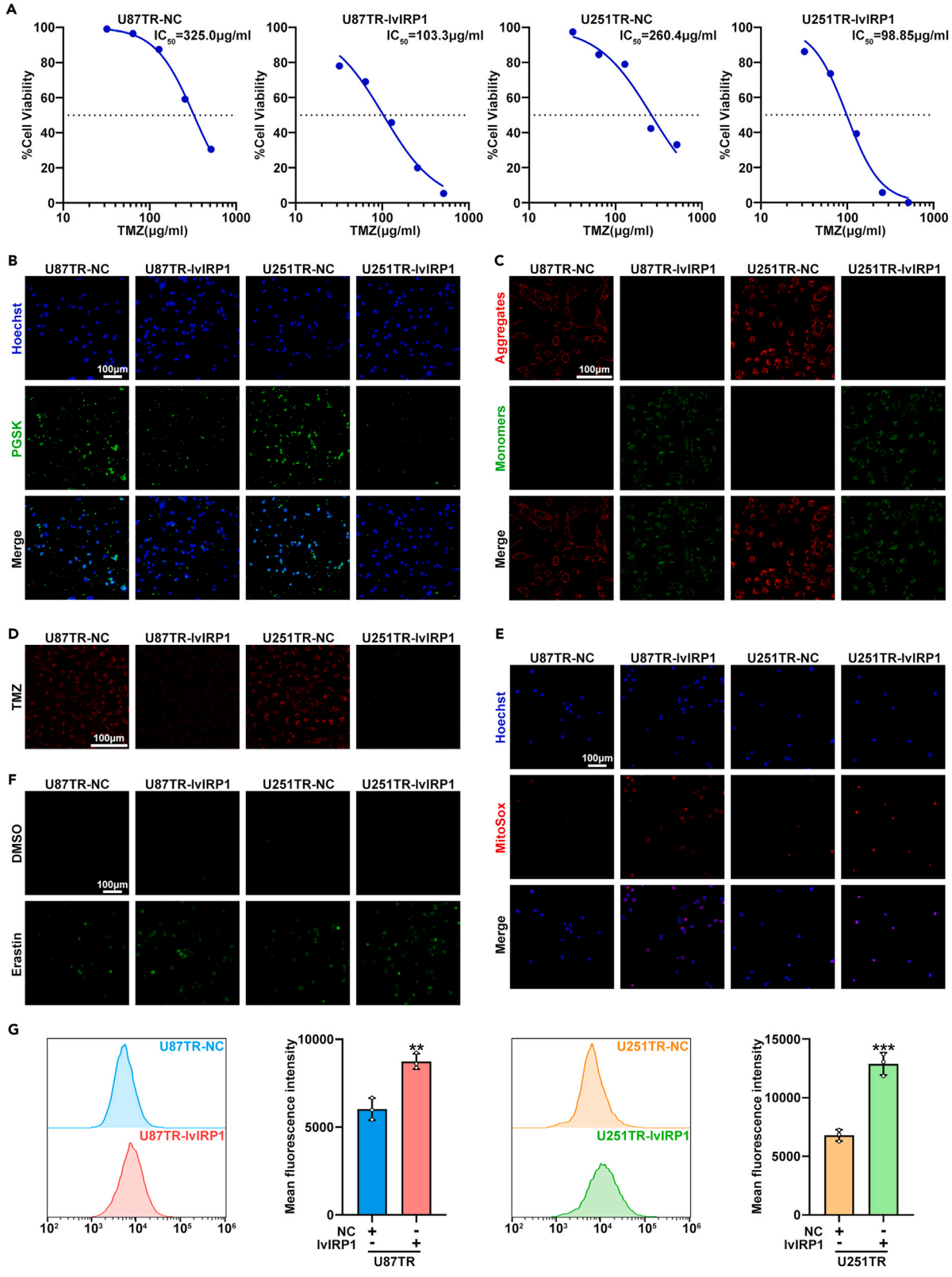
A
U87TR-NC
IC50=325.0μg/ml
U87TR-lvIRP1
IC50=103.3μg/ml
U251TR-NC
IC50=260.4μg/ml
U251TR-lvIRP1
IC50=98.85μg/ml
%Cell Viability
TMZ(μg/ml)
B
U87TR-NC
U87TR-lvIRP1
U251TR-NC
U251TR-lvIRP1
Hoechst
PGSK
Merge
100μm
C
Aggregates
Monomers
Merge
D
TMZ
E
Hoechst
MitoSox
Merge
F
DMSO
Erastin
G
U87TR-NC
U87TR-lvIRP1
Mean fluorescence intensity
NC
lvIRP1
U87TR
U251TR-NC
U251TR-lvIRP1
U251TR

Figure 2. Overexpressed IRP1 increases TMZ chemotherapy sensitivity by enhancing ferroptosis, lipid peroxidation and free iron accumulation

(A) The cell survival rate was measured after TMZ treatment in U87TR-NC, U87TR-lvIRP1, U251TR-NC and U251TR-lvIRP1 groups. Data are represented as the mean ± SD (n = 6).

(B) Representative confocal images of the TR and TR-lvIRP1 groups stained with the PGSK (green) probe to assess intracellular iron levels. Scale bar, 100 μm.

(C) Representative confocal images of the TR and TR-lvIRP1 groups stained with the JC-1 probe (Aggregates, red; Monomers, green) to assess mitochondrial membrane potential. Scale bar, 100 μm.

(D) Representative confocal images of the TR and TR-lvIRP1 groups stained with the TMRE (red) dye to assess mitochondrial membrane potential. Scale bar, 100 μm.

(E) Representative confocal images of the TR and TR-lvIRP1 groups stained with the MitoSOX Red reagent (red) to assess mitochondrial ROS levels. Scale bar, 100 μm.

(F) Representative confocal images of the cells treated with erastin (10 μM) for 24 h stained with the DCF-DA (green) dye to assess cellular ROS. Scale bar, 100 μm.

(G) Lipid peroxidation level in TR and TR-lvIRP1 groups was influenced by erastin (10 μM) 24 h assessed by DCF-DA using flow cytometry immunolabelling.

Considering that the most critical factor for the occurrence of ferroptosis is the change of iron, and the most direct regulator on the level of iron is the intracellular iron homeostasis regulatory proteins IRP1 and IRP2. We applied western blot and qRT-PCR assay to measure the levels of IRP1 or IRP2 in parental and TR cells (Figures 1H and 1I; Figure S1H). The results showed that the expression level of IRP1 was significantly down-regulated in TR cells, while the expression level of IRP2 was not significantly changed. Moreover, the qRT-PCR and western blot analysis demonstrated that IRP1 protein level was also down-regulated in human glioma cells U87, U251, LN229, A172, U118, T98, N9 and N33 compared to normal human astrocytes (NHA) in culture (Figures S1I–S1K), which also reflected that IRP1 may be related to the progression of glioma.

Furthermore, the TCGA database analysis showed that down-regulation of IRP1 was more unfavorable to the survival prognosis of glioma (Figure 1J), while IRP2 had no significant effect on the survival prognosis of glioma (Figure S1L). We therefore focused on IRP1, which was also evident in our data. In addition, immunofluorescence staining showed that IRP1 was mainly localized within the cytoplasm of the parental and TR cells, and its expression in TR cells was significantly down regulated (Figure S1M).

Taken together, these results indicated that reduced IRP1 expression might have an important role in TMZ resistance and served as a novel prognostic marker.

IRP1 is involved in the regulation of ferroptosis, which is associated with chemotherapy sensitivity

In order to investigate whether IRP1 inhibition mediates the resistance of TR cells to ferroptosis. Firstly, we overexpressed IRP1 in TR cells and observed the changes of their sensitivity to ferroptosis. Western blot and qRT-PCR results showed that the overexpression was successful in U87TR-lvIRP1 and U251TR-lvIRP1 groups (Figures S2A and S2B). We found that the IC_{50} value of TMZ was significantly decreased in TR-lvIRP1 groups compared to TR groups, which proved that IRP1 was indeed involved in the change of TMZ resistance in GBM cells (Figure 2A). The relative level of ferrous iron was also increased, indicating that intracellular ferrous iron was upregulated with overexpression of IRP1 (Figure S2C).

We also found that after TMZ treatment, in TR and TR-lvIRP1 cells stained with PGSK probe, the green fluorescence of TR cells overexpressed IRP1 was significantly reduced (Figure 2B), which also reflected that overexpression of IRP1 could reverse the TMZ resistance to a certain extent in TR cells. Moreover, the amount of MDA increased, which indicated that IRP1 overexpression cells had significantly higher lipid oxidation levels and more oxidative damage (Figure S2D). The GSH and GSSG levels also proved that the IRP1 overexpression cells were more sensitive to ferroptosis (Figures S2E and S2F).

We further detected the situation of changes on mitochondrial membrane potential in TR and TR-lvIRP1 cells through JC-1 and TMRE assay after inducing ferroptosis (Figures 2C and 2D). The results indicated that overexpression of IRP1 reversed the innate insensitivity of TR cells to ferroptosis. Confocal images showed that IRP1 overexpression cells were more prone to superoxide production, suggesting that they were more sensitive to ferroptosis than TR cells (Figure 2E). Finally, both the confocal images and flow cytometry results showed that IRP1 overexpression cells could significantly increase the ROS level than TR cells (Figures 2F and 2G). The statistical result of the DCF-DA positive ratio was also shown on the right.

In summary, these results suggest that overexpression of IRP1 increased TMZ chemotherapy sensitivity by enhancing ferroptosis, lipid peroxidation and free iron accumulation.

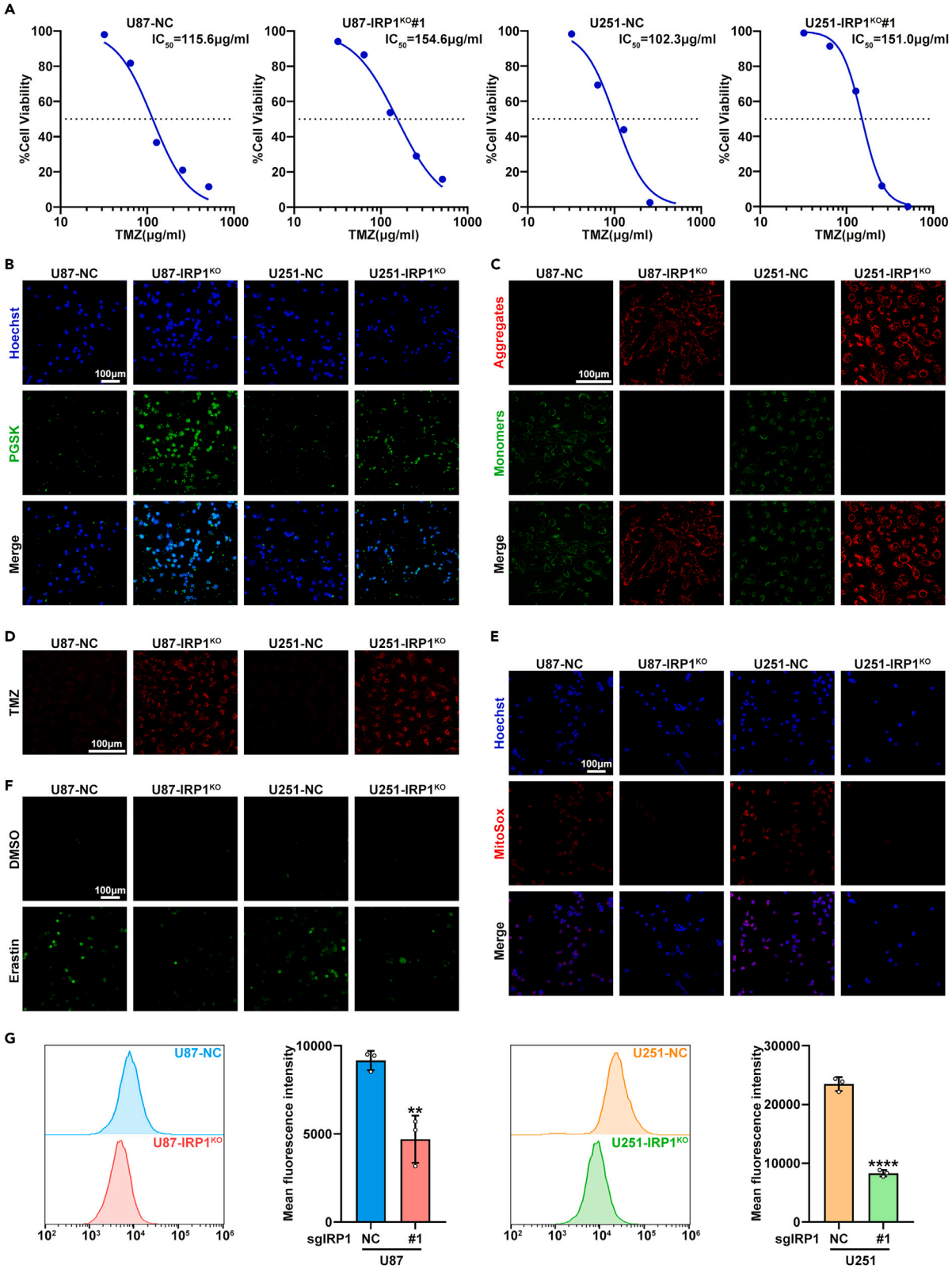
A
U87-NC
IC50=115.6μg/ml
U87-IRP1KO#1
IC50=154.6μg/ml
U251-NC
IC50=102.3μg/ml
U251-IRP1KO#1
IC50=151.0μg/ml
%Cell Viability
TMZ(μg/ml)
B
U87-NC
U87-IRP1KO
U251-NC
U251-IRP1KO
Hoechst
PGSK
Merge
100μm
C
Aggregates
Monomers
D
TMZ
E
MitoSox
F
DMSO
Erastin
G
Mean fluorescence intensity
sgIRP1
NC
#1
U87
U251

Figure 3. Knockout of IRP1 reduced chemotherapy sensitivity by inhibiting ferroptosis, lipid peroxidation, and free iron accumulation

(A) The cell survival rate was measured after TMZ treatment in U87NC, U87KO, U251NC and U251KO groups. Data are represented as the mean ± SD (n = 6).

(B) Representative confocal images of the NC and KO groups stained with the PGSK (green) probe to assess intracellular iron levels. Scale bar, 100 μm.

(C) Representative confocal images of the NC and KO cells stained with the JC-1 probe (Aggregates, red; Monomers, green) to assess mitochondrial membrane potential. Scale bar, 100 μm.

(D) Representative confocal images of the NC and KO cells stained with the TMRE (red) dye to assess mitochondrial membrane potential. Scale bar, 100 μm.

(E) Representative confocal images of the NC and KO groups stained with the MitoSOX Red reagent (red) to assess mitochondrial ROS levels. Scale bar, 100 μm.

(F) Representative confocal images of the sgRNA-IRP1#1 transfected group and the sgRNA-IRP1#1 non-transfected group treated with erastin (10 μM) for 24 h stained with the DCF-DA (green) dye to assess cellular ROS. Scale bar, 100 μm.

(G) Lipid peroxidation level in the sgRNA-IRP1#1 transfected group and the sgRNA-IRP1#1 non-transfected group assessed by DCF-DA using flow cytometry immunolabelling.

IRP1 knockout affects the regulation of ferroptosis, which is associated with chemotherapy sensitivity

The mRNA and protein levels of IRP1 were markedly decreased on qRT-PCR and western blot in U87 and U251 cells transfected with three independent IRP1 cas9-sgRNAs (Figures S3A and S3B). We found that the IC_{50} value of TMZ was significantly increased in IRP1-KO groups compared to NC groups (Figure 3A; Figure S3C), which also demonstrated that IRP1 could play an inhibiting role in the process of TMZ resistance in GBM cells. And, as we expect, the level of ferrous iron was also decreased in sg-IRP1# transfected cells during the induction of ferroptosis (Figure S3D).

The PGSK probe staining showed that the cells transfected with sgRNA-IRP1#1 were less to develop changes in iron level after TMZ treatment, which also indicated that knockout of IRP1 could confer TMZ resistance (Figure 3B). Moreover, corresponding changes in MDA levels were also observed. sg-IRP1# transfected cells were less susceptible to erastin-induced lipid peroxidation and oxidative damage (Figure S3E). Obviously, IRP1 knockout also altered the levels of GSH and GSSG upon ferroptosis induction, the GSH level decreased significantly in sg-IRP1# transfected cells compared with control cells, and the GSSG level increased significantly compared with control cells (Figures S3F and S3G).

The decrease of mitochondrial membrane potential also proved that the mitochondrial membrane potential of sgRNA-IRP1#1 transfected group was less prone to decrease and it maintained their normal mitochondrial function under either TMZ treatment or ferroptosis inducer treatment (Figures 3C and 3D). We further demonstrated that the degree of superoxide production by mitochondria decreased significantly in the sgRNA-IRP1#1 transfected group with the same stimulation (Figure 3E). The confocal images of DCF-DA showed that sgRNA-IRP1#1 transfected group were less susceptible to the influence of generating ROS by ferroptosis inducer. The flow cytometry results and its statistical results were consistent with the confocal results (Figures 3F and 3G).

In conclusion, the knockout of IRP1 can promote the sensitivity to TMZ chemotherapy in GBM cells, which indicates IRP1 may serve as a potential target gene for improving TMZ sensitivity.

Knockout of IRP1 activates the noncanonical NF-κB pathway through NFKB2

To determine whether downregulated IRP1 confers TMZ resistance in GBM cells as a potential mechanism, RNA sequencing analysis was performed to predict possible target genes and enriched pathways. After knocking out IRP1, the RNA-seq results revealed that NFKB1 and NFKB2 were highly expressed, especially NFKB2 (Figures 4A and 4B), and it was predicted to be the highly possible downstream target gene of IRP1 in GBM cells. Moreover, the pathway enrichment analysis by KEGG revealed that the NF-κB pathway was activated extremely (Figure 4C). As one of the five subunits of the mammalian NF-κB family, NFKB2 mainly participates in and regulates noncanonical NF-κB pathway. Western Blot showed that for the canonical NF-κB signaling pathway, the effect of IRP1 KO on it was not obvious (Figure 4D). However, knockout of IRP1 activated the noncanonical NF-κB signaling pathway and significantly increased the expression levels of downstream target genes, such as NFKB2, RelB, IKKα, and Phospho-IKKα (Figure 4E). As expected, the Western Blot results of parental and TR cells also showed the same trend (Figures S4A and S4B). TCGA database analysis showed that glioma patients with high NFKB2 expression level had a worse prognosis, while NFKB1 had no significant effect on the survival prognosis of glioma patients (Figure S4C). We therefore focused on NFKB2 and the noncanonical NF-κB pathway it regulates.

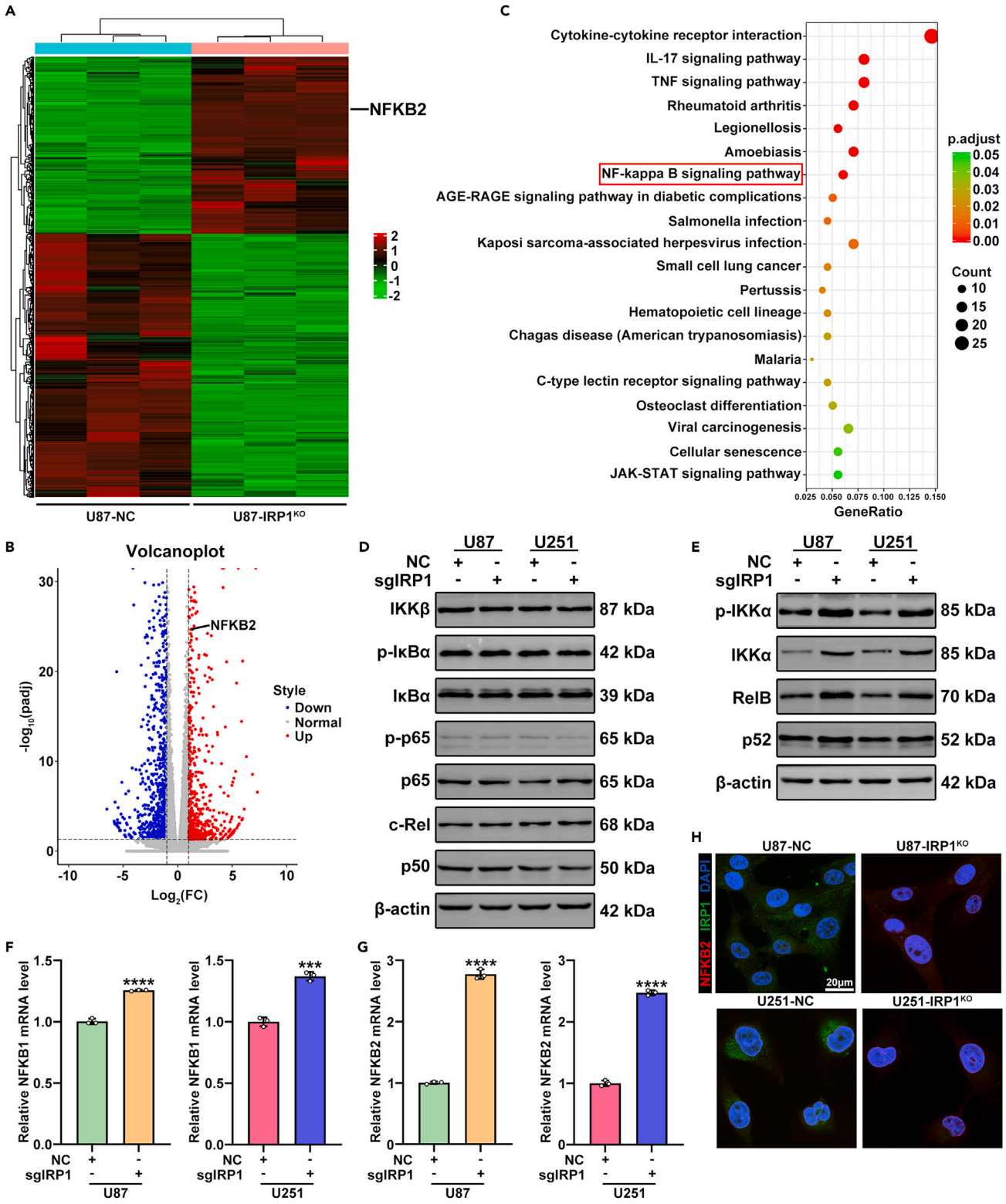

Figure 4. Knockout of IRP1 activates the noncanonical NF-κB pathway through NFKB2

(A) Clustering heatmap of mRNA from the NC and KO cells on the basis of differential expression analysis. Control group: n = 3; IRP1 KO group: n = 3.

(B) Volcano plot displays differential genes expression in U87KO cells. Up (red), down (blue).

(C) KEGG pathway analysis of upregulated genes. Tops of enriched pathway are shown.

Figure 4. *Continued*
(D) Western blot to detect major protein levels in the canonical NF-κB pathway in U87NC, U87KO, U251NC and U251KO cells.
(E) Western blot to detect major protein levels in the noncanonical NF-κB pathway in U87NC, U87KO, U251NC and U251KO cells.
(F) qRT-PCR to detect the NFKB1 mRNA levels in U87NC, U87KO, U251NC and U251KO cells.
(G) qRT-PCR to detect the NFKB2 mRNA levels in U87NC, U87KO, U251NC and U251KO cells.
(H) IF confocal images of IRP1 (green), NFKB2 (red), and nuclei (blue). Scale bar, 20 μm.

Moreover, compared with NFKB1, NFKB2 mRNA expression level was correspondingly higher in both KO cells and TR cells compared to NC cells and parental cells (Figures 4F and 4G; Figures S4D and S4E). Immunofluorescence confocal was used to identify the intracellular localization of IRP1 and NFKB2, and the expression level of NFKB2 in IRP1 KO cells was significantly higher than that in NC cells (Figure 4H).

All in all, these results suggest that downregulated IRP1 promotes chemotherapy resistance through NFKB2-mediated the noncanonical NF-κB signaling pathway activation, not the canonical one.

Knockdown of NFKB2 enhanced ferroptosis sensitivity and reversed TMZ resistance

To determine whether NFKB2 expression is involved in regulating the sensitivity to TMZ, we transfected shRNA targeted NFKB2 into IRP1-KO cells (Figures S5A and S5B). The IC_{50} values of TMZ in NFKB2-targeted cells were calculated, and the results showed that NFKB2 knockdown indeed increased the sensitivity to TMZ in GBM cells (Figure 5A). The PGSK confocal images also showed that cells with IRP1 knockout and NFKB2 knockdown at the same time were more susceptible to iron level changes after TMZ treatment compared with only IRP1 knockout cells (Figure 5B). After treated with ferroptosis inducer, the intracellular ferrous iron levels in NFKB2-targeted cells were significantly higher than that in the control groups in IRP1-KO cells (Figure S5C), and the MDA levels of NFKB2 knockdown groups, the metabolite of lipid peroxidation, also showed an upward trend (Figure S5D). Knocking down NFKB2 resulted in a more significant decrease in GSH level and a more significant increase in GSSG level, both of which indicated that NFKB2 knockdown enhanced sensitivity to ferroptosis (Figures S5E and S5F).

The results of JC-1 images and TMRE images demonstrated that knocking down NFKB2 in IRP1 knockout cells could indeed reverse the feature that KO cells were not susceptible to mitochondrial membrane potential decline with TMZ treatment or ferroptosis inducer treatment, which further confirmed that NFKB2 was a downstream target gene of IRP1 (Figures 5C and 5D), and knockdown of NFKB2 enhanced the sensitivity to ferroptosis and even reversed TMZ resistance. Moreover, the MitoSOX confocal images also indicated that mitochondria in IRP1-KO cells with NFKB2 knockdown were more susceptible to ferroptosis induced superoxide production than in IRP1-KO cells without NFKB2 knockdown (Figure 5E). DCF-DA confocal images showed that targeting NFKB2 made cells more susceptible to ferroptosis inducers to produce ROS (Figure 5F). The flow cytometry results and its statistical results were consistent with the above results (Figure 5G).

Collectively, these data reveal a previously unappreciated link between IRP1 and NFKB2, and lay a foundation for further exploration of the TMZ resistance mechanism of the combination of the two genes.

High expression of NFKB2 activates LCN2/FPN1 to mediate ferroptosis resistance in GBM cells

To further explore the mechanism of IRP1-mediated NFKB2 regulation in TMZ resistance, we considered whether the end of the regulatory axis was related to cellular iron ion transport. By analyzing the survival prognosis of glioma in TCGA database, we found two iron transport-related proteins, LCN2 and FPN1, which were significantly related to the prognosis of glioma. The prognosis of glioma patients with high expression of LCN2 and FPN1 is poor (Figure S6A). As a result, we focused on these two independent poor prognostic markers.

To determine whether LCN2 and FPN1 play an essential role in mediating ferroptosis resistance and act as downstream targeted genes of NFKB2, we firstly performed western blot and qRT-PCR assay on the IRP1-KO groups. The results showed that the expression levels of LCN2 and FPN1 were significantly increased in the cells transfected with sgRNA-IRP1#1 virus particle (Figures 6A–6C). And then, we also detected on the TR groups, as expected, the expression levels of both LCN2 and FPN1 were significantly increased in TR cells (Figures S6B–S6D).

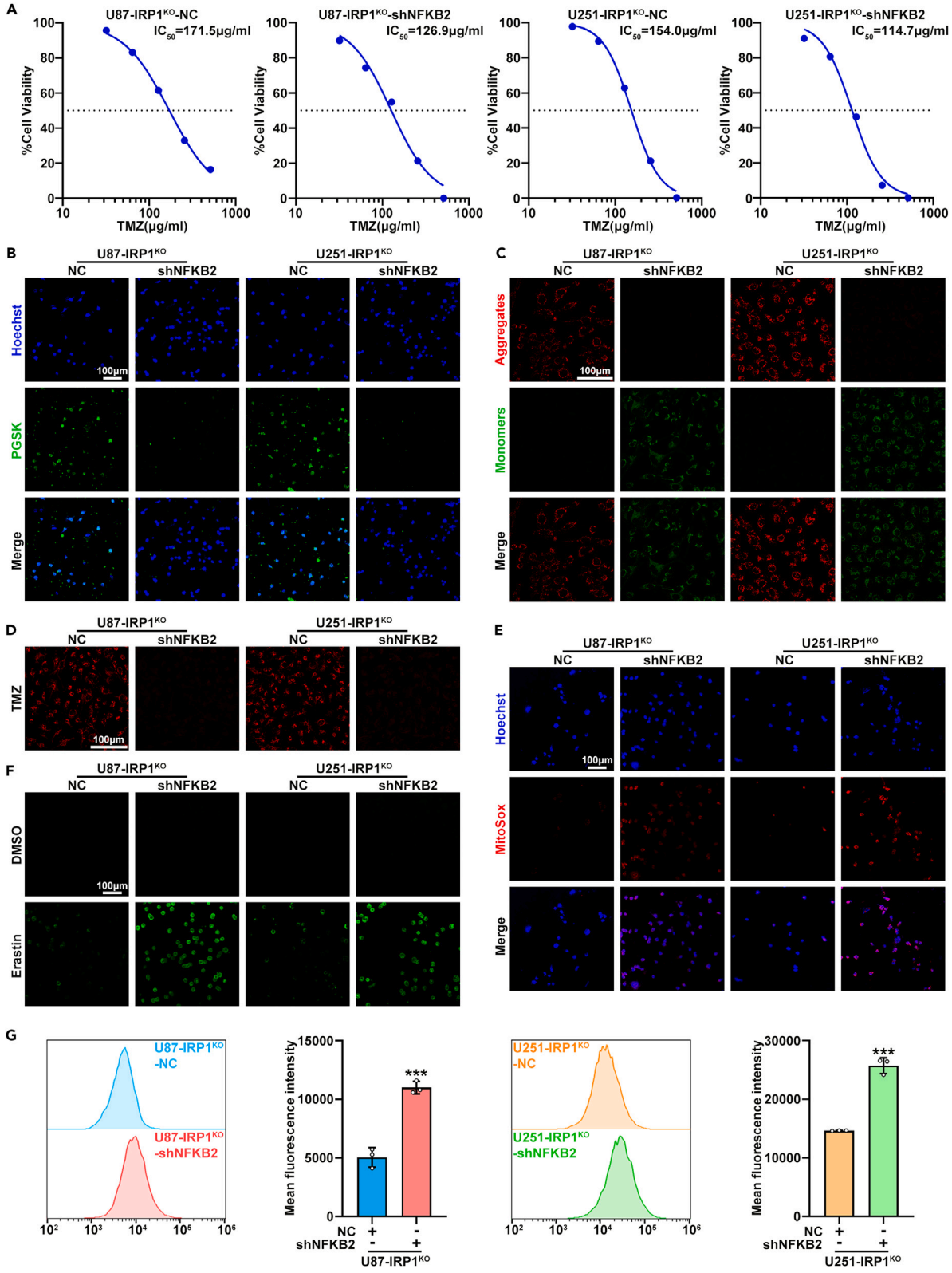
A
U87-IRP1KO-NC
IC50=171.5μg/ml
U87-IRP1KO-shNFKB2
IC50=126.9μg/ml
U251-IRP1KO-NC
IC50=154.0μg/ml
U251-IRP1KO-shNFKB2
IC50=114.7μg/ml
%Cell Viability
TMZ(μg/ml)
B
C
U87-IRP1KO
U251-IRP1KO
NC
shNFKB2
Hoechst
PGSK
Merge
Aggregates
Monomers
100μm
D
TMZ
E
MitoSox
F
DMSO
Erastin
G
U87-IRP1KO -NC
U87-IRP1KO -shNFKB2
U251-IRP1KO -NC
U251-IRP1KO -shNFKB2
Mean fluorescence intensity
***

Figure 5. Knockdown of NFKB2 enhanced ferroptosis sensitivity and reversed TMZ resistance

(A) The cell survival rate was measured after TMZ treatment in U87KO-NC, U87KO-shNFKB2, U251KO-NC and U251KO-shNFKB2 groups. Data are represented as the mean ± SD (n = 6).

(B) Representative confocal images of the IRP1-KO-NC and IRP1-KO-shNFKB2 groups stained with the PGSK (green) probe to assess intracellular iron levels. Scale bar, 100 μm.

(C) Representative confocal images of the IRP1-KO-NC and IRP1-KO-shNFKB2 groups stained with the JC-1 probe (Aggregates, red; Monomers, green) to assess mitochondrial membrane potential. Scale bar, 100 μm.

(D) Representative confocal images of the IRP1-KO-NC and IRP1-KO-shNFKB2 groups stained with the TMRE (red) dye to assess mitochondrial membrane potential. Scale bar, 100 μm.

(E) Representative confocal images of the IRP1-KO-NC and IRP1-KO-shNFKB2 groups stained with the MitoSOX Red reagent (red) to assess mitochondrial ROS levels. Scale bar, 100 μm.

(F) Representative confocal images of the shRNA-NFKB2 transfected group and the shRNA-NFKB2 non-transfected group treated with erastin (10 μM) for 24 h stained with the DCF-DA (green) dye to assess cellular ROS. Scale bar, 100 μm.

(G) Lipid peroxidation level in the shRNA-NFKB2 transfected group and the shRNA-NFKB2 non-transfected group assessed by DCF-DA using flow cytometry immunolabelling.

Cells overexpressed NFKB2 were obtained from parental GBM cells transfected with lv-NFKB2 virus particle (Figures S6E and S6F). The results of western blot and qRT-PCR demonstrated that the expression levels of LCN2 and FPN1 were increased correspondingly with overexpression of NFKB2 (Figures 6D–6F). And we used chromatin immunoprecipitation (ChIP) assay to confirm that NFKB2 was capable of binding to the promoter regions of LCN2 and FPN1 in the U87 cells (Figure 6G). In addition, the changes of ferrous iron, MDA and DCF levels in NFKB2 overexpressed cells were detected to evaluate the effect of NFKB2 on intracellular iron level and lipid peroxidation level (Figures 6H–6J).

To determine whether NFKB2 acts as an upstream gene for activating LCN2 and FPN1, we performed a series of verification experiments in IRP1-KO cells with NFKB2 knockdown. The results of western blot and qRT-PCR demonstrated that knocking down NFKB2 could decrease the expression level of LCN2 and FPN1 in IRP1-KO cells (Figures 6K–6M) Due to the iron transport function of LCN2 and FPN1, the change of their expression will further lead to the decrease or increase of intracellular iron level. Correspondingly to the change in LCN2 and FPN1 expression, the levels of Ferrous iron, MDA and DCF were partly rescued in IRP1-KO cells with NFKB2 knockdown (Figures 6N–6P).

These results confirmed our hypothesis that LCN2 and FPN1 were indeed the downstream targeted genes of the IRP1/NFKB2 axis in regulating ferroptosis sensitivity and TMZ resistance in GBM cells.

Overexpressed IRP1 enhances ferroptosis-based TMZ antitumor therapy *in vivo*

To further investigate the role of IRP1 on the efficacy of TMZ *in vivo*, an orthotopic GBM mice model was generated by intracranially injecting the two groups of cells separately into mice brains. Then, mice were intraperitoneally injected with DMSO or TMZ (5 mg/kg/day) at the frequency of 5 days on and 2 days off for 2 weeks (Figure 7A).

The bioluminescence imaging and changes in mice body weight indicated that those tumors established with U87TR-lvIRP1 cells were more sensitive to TMZ treatment when compared to U87TR group (Figures 7B–7D). Kaplan-Meier survival curves showed that the median survival time of the mice was 34 days in the U87TR group, 42 days in the U87TR + TMZ group, and 35 days in the U87TR-lvIRP1 group, while the U87TR-lvIRP1+TMZ group extended the median survival time to 55 days (Figure 7E).

In addition, H&E staining confirmed that the tumor volume of the U87TR-lvIRP1+TMZ group was significantly smaller than that of the U87TR + TMZ group (Figure 7F). Ki67 staining also indicated that the percentage of proliferating cells in the U87TR-lvIRP1+TMZ group was lower than that in the U87TR + TMZ group (Figure 7G). We also examined ferrous iron and MDA levels in orthotopic tumors of xenograft model, and the results showed that ferrous iron and MDA levels in the U87TR-lvIRP1+TMZ group were significantly higher compared to those in other groups, which also confirmed that U87TR-lvIRP1 cells were more sensitive to TMZ-induced changes in iron levels and lipid peroxidation (Figures 7H and 7I).

Together, these results strongly revealed that IRP1 enhanced TMZ antitumor therapy based on ferroptosis *in vivo* and that IRP1 could be a potential therapy target for overcoming chemoresistance.

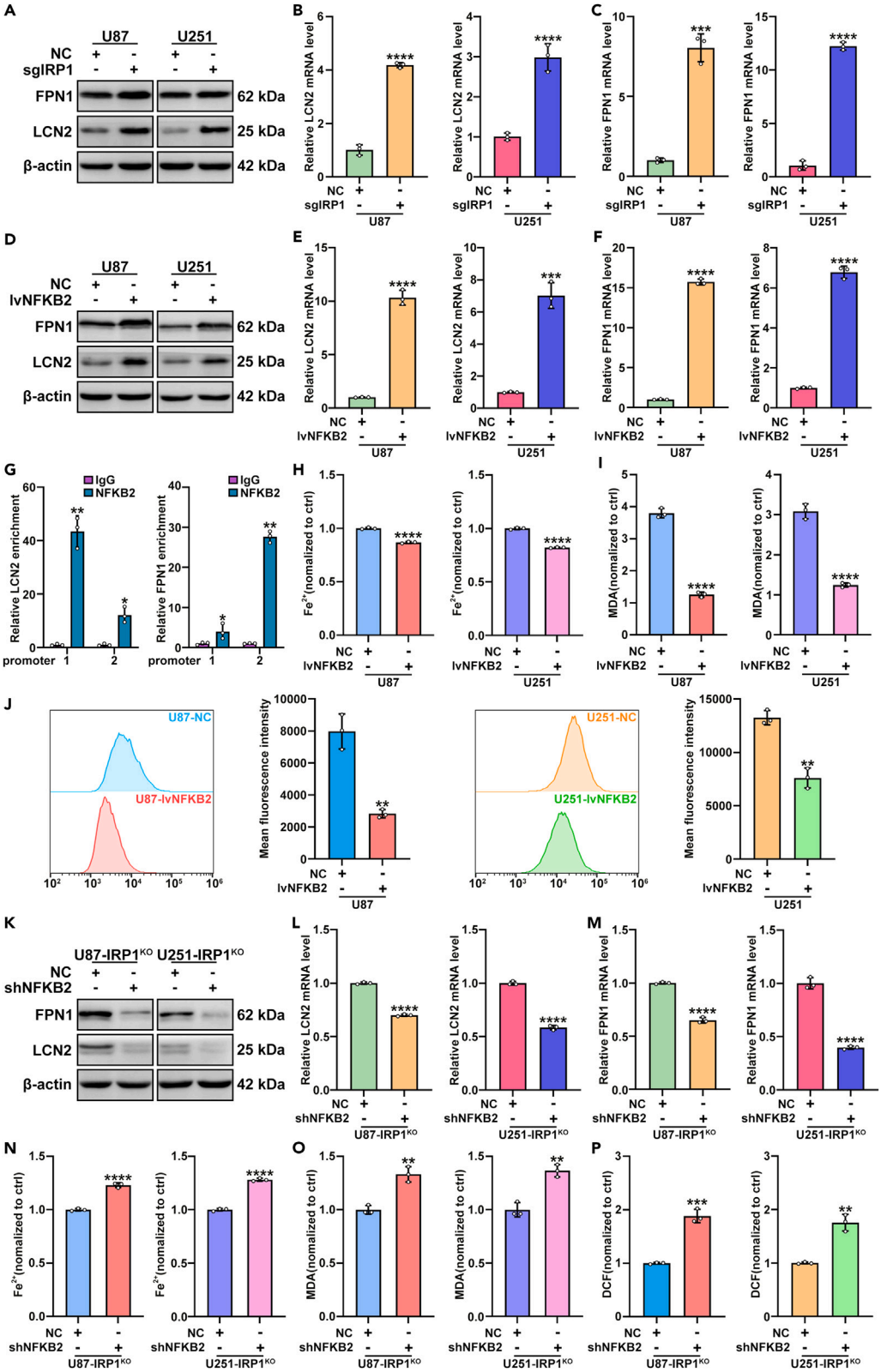
A
U87
U251
NC
sgIRP1
FPN1
LCN2
β-actin
62 kDa
25 kDa
42 kDa
B
Relative LCN2 mRNA level
C
Relative FPN1 mRNA level
D
lvNFKB2
E
F
G
IgG
NFKB2
Relative LCN2 enrichment
Relative FPN1 enrichment
promoter 1
promoter 2
H
Fe2+(nomalized to ctrl)
I
MDA(nomalized to ctrl)
J
U87-NC
U87-lvNFKB2
U251-NC
U251-lvNFKB2
Mean fluorescence intensity
K
U87-IRP1KO
U251-IRP1KO
shNFKB2
L
M
N
O
P
DCF(nomalized to ctrl)

Figure 6. High expression of NFKB2 activates LCN2/FPN1 to mediate ferroptosis resistance in GBM cells

(A) Western Blot analysis detected the expression of LCN2 and FPN1 in IRP1-NC and IRP1-KO cells.
(B and C) qRT-PCR detected the expression of LCN2 and FPN1 in IRP1-NC and IRP1-KO cells.
(D) Western Blot analysis to detect NFKB2 protein levels in parental cells transfected with lv-NFKB2.
(E and F) qRT-PCR detected the expression of LCN2 and FPN1 in NC and lvNFKB2 cells.
(G) ChIP assay of the enrichment of NFKB2 in the LCN2 and FPN1 promoter region normalized to IgG in U87 cells.
(H) Ferrous iron levels detected after overexpression of NFKB2 in parental cells.
(I) MDA levels detected after overexpression of NFKB2 in parental cells.
(J) DCF levels detected after overexpression of NFKB2 in parental cells.
(K) Western Blot analysis detected the expression of LCN2 and FPN1 in IRP1-KO-NC and IRP1-KO-shNFKB2 cells.
(L and M) qRT-PCR detected the expression of LCN2 and FPN1 in IRP1-KO-NC and IRP1-KO-shNFKB2 cells.
(N) Ferrous iron levels detected after knockdown of NFKB2 in IRP1-KO cells.
(O) MDA levels detected after knockdown of NFKB2 in IRP1-KO cells.
(P) DCF levels detected after knockdown of NFKB2 in IRP1-KO cells.

DISCUSSION

TMZ administration significantly prolongs the median survival time, but almost all GBM patients eventually develop TMZ resistance during the course of the treatment.[7] Previous studies have shown TMZ resistance as a multifactorial process that occurs by a variety of cell mechanisms. Activation of DNA repair pathways is the principal mechanism for this phenomenon that detaches TMZ-induced O-6-methylguanine adducts and restores genomic integrity.[28] Current understanding in the domain of oncology reveals several other novel mechanisms of resistance, such as the involvement of miRNAs, drug efflux transporters, gap junction's activity, the advent of glioma stem cells as well as appearance of cell autophagy.[29] Substantial evidences have been obtained over the past decades that changes in iron uptake and iron management are essential features of tumor cells. Alterations in iron metabolism are now recognized as a key metabolic "hallmark" of cancer.[9] Reprogramming of iron metabolism and dysfunction of iron homeostasis have also been found in GBM.[30]

Ferroptosis, a form of non-apoptotic cell death, has attracted much attention in recent years as a potential anti-tumor strategy to overcome apoptotic resistance. More and more studies have begun to explore new ways to treat gliomas through lipid peroxidation and oxidative stress in the ferroptosis mechanism.[31,32] Emerging evidences suggested that some oncogenic pathways are associated with ferroptosis, making cancer cells highly susceptible to death, and ferroptosis has recently been identified as a natural tumor suppressor mechanism; like inactivation of apoptosis, its inactivation contributes to tumor development.[33] Recent studies have found that the metabolic plasticity of tumor cells plays an important role in the persistence, dedifferentiation, and expansion of tumor cells. In some cases, the metabolic reprogramming has been associated with acquired sensitivity to ferroptosis, thus opening up new opportunities to treat tumors that are resistant to chemotherapy. However, it remains unclear what metabolic determinants are critical for treatment resistance and evasion of immune surveillance.[34] Due to the paucity of research in ferroptosis and TMZ resistance, we aimed to investigate the molecular mechanisms of ferroptosis in TMZ resistance, in order to find a new regulatory axis that can reverse TMZ sensitivity.

In our study, we focused on IRP1, a well-known iron regulatory protein, cause it is an important element in the regulation of iron homeostasis in animal cells.[35] Previous investigators found that overexpressed IRP1 was associated with a pronounced tumor suppressor phenotype and provided a direct regulatory link between the IRE/IRP system and cancer.[36] By analyzing the survival prognosis of glioma patients in TCGA database, we found that glioma patients with high expression of IRP1 had better survival prognosis (Figure 1J). We also found that IRP1 was down-regulated in TMZ-resistant GBM cells (Figure 1I), which revealed that IRP1 expression was associated with TMZ resistance. Our *in vitro* experiments confirmed that the alteration of IRP1 expression could affect the TMZ sensitivity of GBM cells. To further explore the downstream mechanism of IRP1 in regulating TMZ resistance, RNA-seq was performed in U87 cells with IRP1 knockout. Based on sequencing results, the downstream target gene NFKB2 and the noncanonical NF-κB regulatory pathway were identified. Activation of the noncanonical NF-κB pathway involves different signaling molecules and leads to the predominant activation of the p52/RelB dimer, which based on processing of p100, the NFKB2 precursor protein.[37] Of note, the research on the key gene NFKB2 in the non-classical pathway and TMZ resistance in glioma does not exist, therefore, our study is a groundbreaking work. Our results confirmed that FPN1 and LCN2 could act as downstream targeted gene of the IRP1/NFKB2 regulatory axis to affect ferroptosis sensitivity and TMZ resistance in GBM cells. Furthermore, our *in vivo* experiments also fully demonstrated that overexpressed IRP1 could reverse TMZ resistance, significantly enhance the therapeutic efficacy of TMZ.

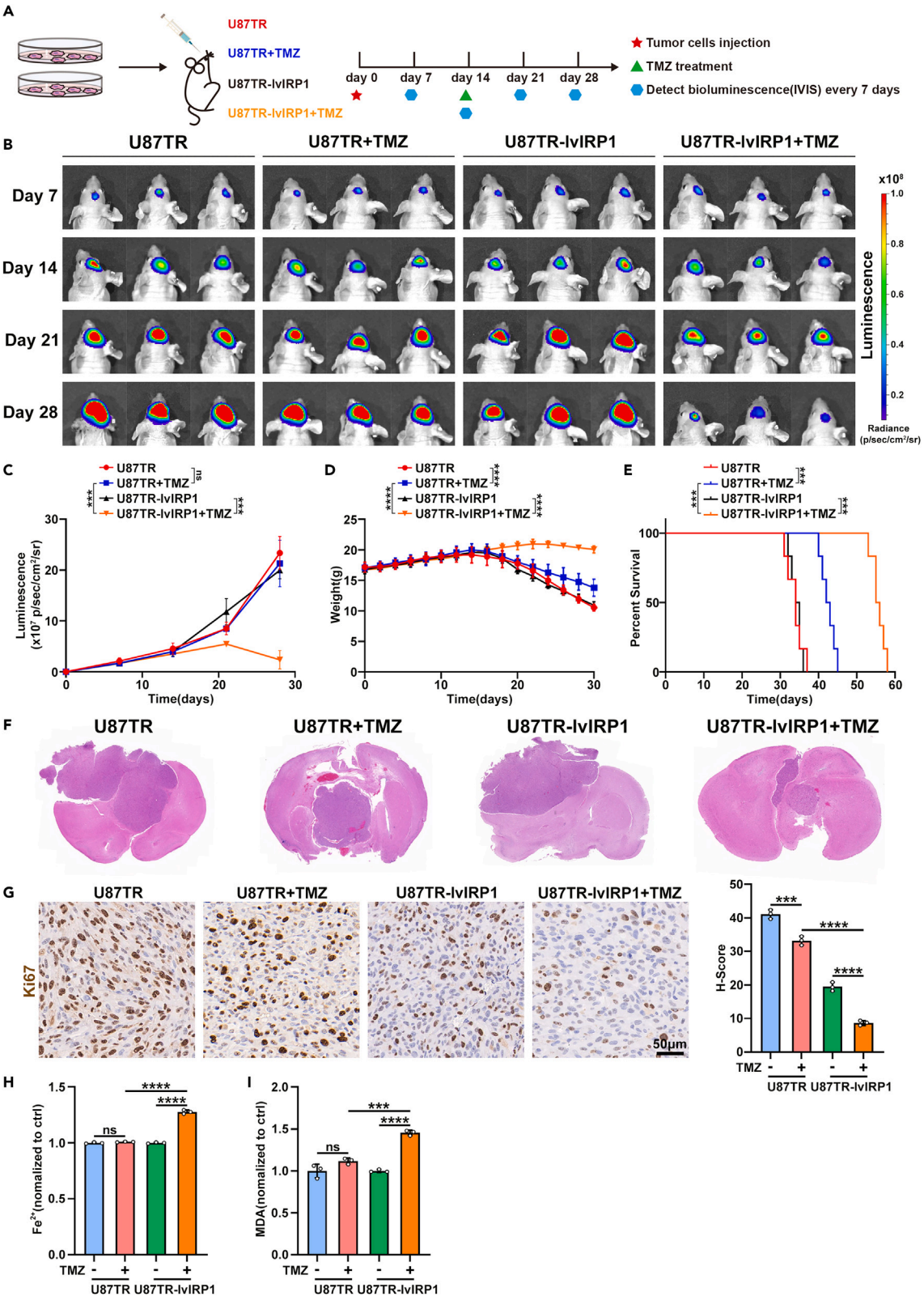
A
U87TR
U87TR+TMZ
U87TR-lvIRP1
U87TR-lvIRP1+TMZ
day 0
day 7
day 14
day 21
day 28
Tumor cells injection
TMZ treatment
Detect bioluminescence(IVIS) every 7 days
B
U87TR
U87TR+TMZ
U87TR-lvIRP1
U87TR-lvIRP1+TMZ
Day 7
Day 14
Day 21
Day 28
x10⁸
Luminescence
Radiance (p/sec/cm²/sr)
C
Luminescence (x10⁷ p/sec/cm²/sr)
Time(days)
D
Weight(g)
Time(days)
E
Percent Survival
Time(days)
F
G
Ki67
50μm
H-Score
TMZ
U87TR U87TR-lvIRP1
H
Fe²⁺(nomalized to ctrl)
I
MDA(nomalized to ctrl)

Figure 7. Overexpressed IRP1 enhances ferroptosis-based TMZ antitumor therapy *in vivo*

(A) Schematic illustration of the GBM orthotopic xenograft model.
(B) Bioluminescence images of tumor growth after tumor implantation. n = 6 for each group.
(C) Tumor growth curves by quantification of bioluminescent imaging signal intensities. Data were represented as the mean ± SD (n = 6).
(D) Mice body weight curves started with the generation of xenograft model. Data were represented as the mean ± SD (n = 6).
(E) Kaplan-Meier survival curve of nude mice. Data are represented as the mean ± SD (n = 6).
(F) Representative images of H&E staining showing tumor volume in the nude mice.
(G) IHC staining for Ki67 in brain tumor samples. Scale bar, 50 μm.
(H) Relative level of Ferrous iron in brain tumor samples.
(I) Relative level of MDA in brain tumor samples.

In summary, our study demonstrated that IRP1 could confer TMZ resistance to GBM cells by attenuating ferroptosis (Figure 8). These results highlight the new mechanism of TMZ resistance and provide a novel strategy to overcome the acquired TMZ resistance in GBM patients via upregulating IRP1 expression. Importantly, we unprecedentedly demonstrated that IRP1 can act as a tumor suppressor to predict clinical prognosis of GBM patients. In addition, we identified the novel IRP1-NFKB2-LCN2/FPN1 signaling axis which is critical for regulating ferroptosis and cell survival. Our results shed light on the importance of the mechanisms counteracting ferroptosis in chemotherapeutic progression and provide an innovative treatment strategy for GBM patients.

Limitations of the study

While we demonstrated a critical role of IRP1 in mediating TMZ resistance via the noncanonical NF-κB signaling pathway, it is also worth identifying the molecular mechanism by which NFKB2 regulates LCN2 and FPN1 expression. Moreover, the intracranial tumor formation mouse was used to verify the IRP1/LCN2/FPN1 signaling axis, if PDX or organoid model can be used, it will be more convinced. Moreover, the clinical data we used comes from public databases, and it is better to add clinical samples collected by ourselves for verification in our future studies.

STAR★METHODS

Detailed methods are provided in the online version of this paper and include the following:

- KEY RESOURCES TABLE
- RESOURCE AVAILABILITY
  - Lead contact
  - Materials availability
  - Data and code availability
- EXPERIMENTAL MODEL AND STUDY PARTICIPANT DETAILS

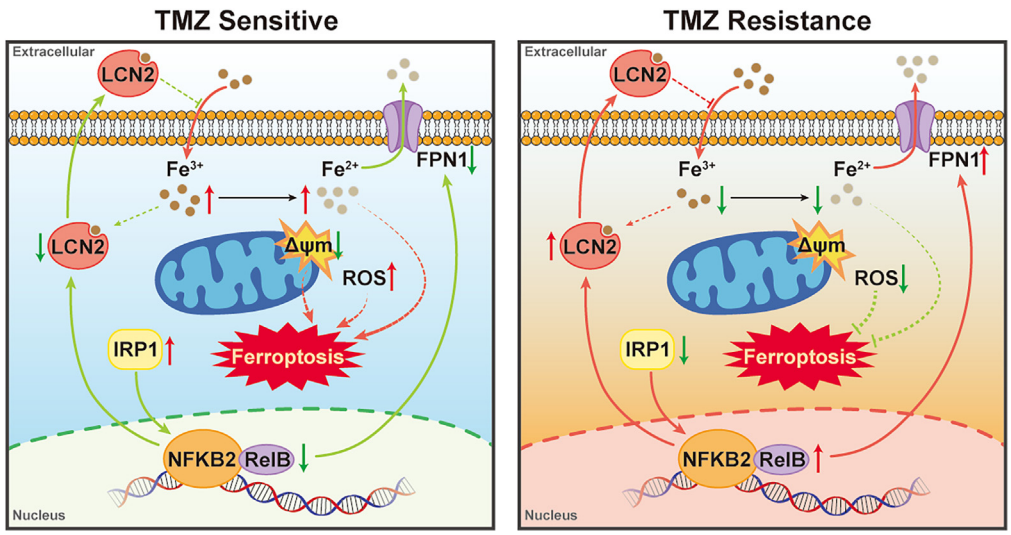

Figure 8. The schematic model describes how ferroptosis which IRP1 mediated affects the progression of TMZ resistance in GBM cells via regulating the noncanonical NF-κB pathway

SUPPLEMENTAL INFORMATION

Supplemental information can be found online at https://doi.org/10.1016/j.isci.2023.107377.

ACKNOWLEDGMENTS

This work was supported by the National Natural Science Foundation of China (82073193, 82102946), Key Area Research and Development Program of Guangdong Province and Guangdong Provincial Clinical Medical Centre for Neurosurgery (No. 2013B020400005).

AUTHOR CONTRIBUTIONS

G.H., L.B., and L.Y. designed the study. L.Y., Y.T., Y.Q., W.Z., Z.X., L.X., Z.B., Z.M., and Z.T. carried out the experiments. G.H. and L.B. provided technical support. L.Y. performed data analysis and wrote the manuscript. All authors read and approved the final manuscript.

DECLARATION OF INTERESTS

The authors declare no competing interests.

INCLUSION AND DIVERSITY

We support inclusive, diverse, and equitable conduct of research.

Received: February 6, 2023
Revised: May 6, 2023
Accepted: July 8, 2023
Published: July 12, 2023

REFERENCES

1. Alexander, B.M., and Cloughesy, T.F. (2017). Adult glioblastoma. J. Clin. Oncol. *35*, 2402–2409. https://doi.org/10.1200/jco.2017.73.0119.

2. Lapointe, S., Perry, A., and Butowski, N.A. (2018). Primary brain tumours in adults. Lancet *392*, 432–446. https://doi.org/10.1016/s0140-6736(18)30990-5.

3. Louis, D.N., Perry, A., Wesseling, P., Brat, D.J., Cree, I.A., Figarella-Branger, D., Hawkins, C., Ng, H.K., Pfister, S.M., Reifenberger, G., et al. (2021). The 2021 WHO classification of tumors of the central nervous system: A summary. Neuro Oncol. *23*, 1231–1251. https://doi.org/10.1093/neuonc/noab106.

4. Claus, E.B., and Black, P.M. (2006). Survival rates and patterns of care for patients diagnosed with supratentorial low-grade gliomas: data from the SEER program. Cancer *106*, 1358–1363. https://doi.org/10.1002/cncr.21733.

5. Stupp, R., Hegi, M.E., Mason, W.P., van den Bent, M.J., Taphoorn, M.J.B., Janzer, R.C., Ludwin, S.K., Allgeier, A., Fisher, B., Belanger, K., et al. (2009). Effects of radiotherapy with concomitant and adjuvant temozolomide versus radiotherapy alone on survival in glioblastoma in a randomised phase III study: 5-year analysis of the EORTC-NCIC trial. Lancet Oncol. *10*, 459–466. https://doi.org/10.1016/s1470-2045(09)70025-7.

6. Tan, A.C., Ashley, D.M., López, G.Y., Malinzak, M., Friedman, H.S., and Khasraw, M. (2020). Management of glioblastoma: State of the art and future directions. CA

Cancer J. Clin. *70*, 299–312. https://doi.org/10.3322/caac.21613.

7. Stupp, R., Mason, W.P., van den Bent, M.J., Weller, M., Fisher, B., Taphoorn, M.J.B., Belanger, K., Brandes, A.A., Marosi, C., Bogdahn, U., et al. (2005). Radiotherapy plus concomitant and adjuvant temozolomide for glioblastoma. N. Engl. J. Med. *352*, 987–996. https://doi.org/10.1056/NEJMoa043330.

8. Legendre, C., and Garcion, E. (2015). Iron metabolism: A double-edged sword in the resistance of glioblastoma to therapies. Trends Endocrinol. Metab. *26*, 322–331. https://doi.org/10.1016/j.tem.2015.03.008.

9. Torti, S.V., and Torti, F.M. (2013). Iron and cancer: More ore to be mined. Nat. Rev. Cancer *13*, 342–355. https://doi.org/10.1038/nrc3495.

10. Chen, X., Kang, R., Kroemer, G., and Tang, D. (2021). Broadening horizons: The role of ferroptosis in cancer. Nat. Rev. Clin. Oncol. *18*, 280–296. https://doi.org/10.1038/s41571-020-00462-0.

11. Chen, J.J., and Galluzzi, L. (2018). Fighting resilient cancers with iron. Trends Cell Biol. *28*, 77–78. https://doi.org/10.1016/j.tcb.2017.11.007.

12. Dixon, S.J., Lemberg, K.M., Lamprecht, M.R., Skouta, R., Zaitsev, E.M., Gleason, C.E., Patel, D.N., Bauer, A.J., Cantley, A.M., Yang, W.S., et al. (2012). Ferroptosis: An iron-dependent form of nonapoptotic cell death. Cell *149*, 1060–1072. https://doi.org/10.1016/j.cell.2012.03.042.

13. Stockwell, B.R., Friedmann Angeli, J.P., Bayir, H., Bush, A.I., Conrad, M., Dixon, S.J., Fulda, S., Gascón, S., Hatzios, S.K., Kagan, V.E., et al. (2017). Ferroptosis: A regulated cell death nexus linking metabolism, redox biology, and disease. Cell *171*, 273–285. https://doi.org/10.1016/j.cell.2017.09.021.

14. Wu, Y., Zhang, S., Gong, X., Tam, S., Xiao, D., Liu, S., and Tao, Y. (2020). The epigenetic regulators and metabolic changes in ferroptosis-associated cancer progression. Mol. Cancer *19*, 39. https://doi.org/10.1186/s12943-020-01157-x.

15. Lei, G., Zhuang, L., and Gan, B. (2022). Targeting ferroptosis as a vulnerability in cancer. Nat. Rev. Cancer *22*, 381–396. https://doi.org/10.1038/s41568-022-00459-0.

16. Zhang, C., Liu, X., Jin, S., Chen, Y., and Guo, R. (2022). Ferroptosis in cancer therapy: A novel approach to reversing drug resistance. Mol. Cancer *21*, 47. https://doi.org/10.1186/s12943-022-01530-y.

17. Gu, Z., Wang, H., Xia, J., Yang, Y., Jin, Z., Xu, H., Shi, J., De Domenico, I., Tricot, G., and Zhan, F. (2015). Decreased ferroportin promotes myeloma cell growth and osteoclast differentiation. Cancer Res. *75*, 2211–2221. https://doi.org/10.1158/0008-5472.CAN-14-3804.

18. Katsarou, A., and Pantopoulos, K. (2020). Basics and principles of cellular and systemic iron homeostasis. Mol. Aspects Med. *75*, 100866. https://doi.org/10.1016/j.mam.2020.100866.

19. Terzi, E.M., Sviderskiy, V.O., Alvarez, S.W., Whiten, G.C., and Possemato, R. (2021). Iron-sulfur cluster deficiency can be sensed by IRP2 and regulates iron homeostasis and sensitivity to ferroptosis independent of IRP1 and FBXL5. Sci. Adv. *7*, eabg4302. https://doi.org/10.1126/sciadv.abg4302.

20. Ganz, T. (2005). Cellular iron: Ferroportin is the only way out. Cell Metab. *1*, 155–157. https://doi.org/10.1016/j.cmet.2005.02.005.

21. Khabibov, M., Garifullin, A., Boumber, Y., Khaddour, K., Fernandez, M., Khamitov, F., Khalikova, L., Kuznetsova, N., Kit, O., and Kharin, L. (2022). Signaling pathways and therapeutic approaches in glioblastoma multiforme (Review). Int. J. Oncol. *60*, 69. https://doi.org/10.3892/ijo.2022.5359.

22. Cahill, K.E., Morshed, R.A., and Yamini, B. (2016). Nuclear factor-kappaB in glioblastoma: Insights into regulators and targeted therapy. Neuro Oncol. *18*, 329–339. https://doi.org/10.1093/neuonc/nov265.

23. Lakhal-Littleton, S., Wolna, M., Carr, C.A., Miller, J.J.J., Christian, H.C., Ball, V., Santos, A., Diaz, R., Biggs, D., Stillion, R., et al. (2015). Cardiac ferroportin regulates cellular iron homeostasis and is important for cardiac function. Proc. Natl. Acad. Sci. USA *112*, 3164–3169. https://doi.org/10.1073/pnas.1422373112.

24. Xu, P., Ge, F.H., Li, W.X., Xu, Z., Wang, X.L., Shen, J.L., Xu, A.B., and Hao, R.R. (2022). MicroRNA-147a targets SLC40A1 to induce ferroptosis in human glioblastoma. Anal. Cell Pathol. *2022*, 2843990. https://doi.org/10.1155/2022/2843990.

25. Chaudhary, N., Choudhary, B.S., Shah, S.G., Khapare, N., Dwivedi, N., Gaikwad, A., Joshi, N., Raichanna, J., Basu, S., Gurjar, M., et al. (2021). Lipocalin 2 expression promotes tumor progression and therapy resistance by inhibiting ferroptosis in colorectal cancer. Int. J. Cancer *149*, 1495–1511. https://doi.org/10.1002/ijc.33711.

26. Morales-Valencia, J., Lau, L., Martí-Nin, T., Ozerdem, U., and David, G. (2022). Therapy-induced senescence promotes breast cancer cells plasticity by inducing Lipocalin-2 expression. Oncogene *41*, 4361–4370. https://doi.org/10.1038/s41388-022-02433-4.

27. Kaplan, J. (2002). Mechanisms of cellular iron acquisition: another iron in the fire. Cell *111*, 603–606. https://doi.org/10.1016/s0092-8674(02)01164-9.

28. Choi, S., Yu, Y., Grimmer, M.R., Wahl, M., Chang, S.M., and Costello, J.F. (2018). Temozolomide-associated hypermutation in gliomas. Neuro Oncol. *20*, 1300–1309. https://doi.org/10.1093/neuonc/noy016.

29. Tomar, M.S., Kumar, A., Srivastava, C., and Shrivastava, A. (2021). Elucidating the mechanisms of Temozolomide resistance in gliomas and the strategies to overcome the resistance. Biochim. Biophys. Acta. Rev. Cancer *1876*, 188616. https://doi.org/10.1016/j.bbcan.2021.188616.

30. Hanahan, D., and Weinberg, R.A. (2011). Hallmarks of cancer: The next generation. Cell *144*, 646–674. https://doi.org/10.1016/j.cell.2011.02.013.

31. Hacioglu, C., and Kar, F. (2023). Capsaicin induces redox imbalance and ferroptosis through ACSL4/GPx4 signaling pathways in U87-MG and U251 glioblastoma cells. Metab. Brain Dis. *38*, 393–408. https://doi.org/10.1007/s11011-022-00983-w.

32. Kar, F., Hacioğlu, C., and Kaçar, S. (2023). The dual role of boron in vitro neurotoxication of glioblastoma cells via SEMA3F/NRP2 and ferroptosis signaling pathways. Environ. Toxicol. *38*, 70–77. https://doi.org/10.1002/tox.23662.

33. Lei, G., Zhang, Y., Koppula, P., Liu, X., Zhang, J., Lin, S.H., Ajani, J.A., Xiao, Q., Liao, Z., Wang, H., and Gan, B. (2020). The role of ferroptosis in ionizing radiation-induced cell death and tumor suppression. Cell Res. *30*, 146–162. https://doi.org/10.1038/s41422-019-0263-3.

34. Friedmann Angeli, J.P., Krysko, D.V., and Conrad, M. (2019). Ferroptosis at the crossroads of cancer-acquired drug resistance and immune evasion. Nat. Rev. Cancer *19*, 405–414. https://doi.org/10.1038/s41568-019-0149-1.

35. Volz, K. (2008). The functional duality of iron regulatory protein 1. Curr. Opin. Struct. Biol. *18*, 106–111. https://doi.org/10.1016/j.sbi.2007.12.010.

36. Chen, G., Fillebeen, C., Wang, J., and Pantopoulos, K. (2007). Overexpression of iron regulatory protein 1 suppresses growth of tumor xenografts. Carcinogenesis *28*, 785–791. https://doi.org/10.1093/carcin/bgl210.

37. Sun, S.C. (2017). The non-canonical NF-kappaB pathway in immunity and inflammation. Nat. Rev. Immunol. *17*, 545–558. https://doi.org/10.1038/nri.2017.52.

38. Zeng, H., Xu, N., Liu, Y., Liu, B., Yang, Z., Fu, Z., Lian, C., and Guo, H. (2017). Genomic profiling of long non-coding RNA and mRNA expression associated with acquired temozolomide resistance in glioblastoma cells. Int. J. Oncol. *51*, 445–455. https://doi.org/10.3892/ijo.2017.4033.

STAR★METHODS

KEY RESOURCES TABLE

REAGENT or RESOURCE	SOURCE	IDENTIFIER
Antibodies		
Rabbit anti-ACO1	Abcam	Cat# ab236773
Mouse anti-IRP2	Santa Cruz Biotechnology	Cat# sc33682; RRID: AB_2126703
Rabbit anti-LCN2	Proteintech	Cat# 26991-1-AP; RRID: AB_2880715
Rabbit anti-FPN1	Proteintech	Cat# 26601-1-AP; RRID: AB_2880571
Rabbit anti-β-actin	Proteintech	Cat# 66009-1-Ig; RRID: AB_2782959
Rabbit anti-NF-κB p65	Cell Signaling Technology	Cat# 8242; RRID: AB_10859369
Rabbit anti-P-NF-κB p65	Cell Signaling Technology	Cat# 3033; RRID: AB_331284
Rabbit anti-RelB	Cell Signaling Technology	Cat# 10544; RRID: AB_2797727
Rabbit anti-c-Rel	Cell Signaling Technology	Cat# 12707; RRID: AB_2721030
Rabbit anti-NF-κB1 p105/50	Cell Signaling Technology	Cat# 13586; RRID: AB_2665516
Rabbit anti-NF-κB2 p100/52	Cell Signaling Technology	Cat# 4882; RRID: AB_10695537
Mouse anti-IKKα	Cell Signaling Technology	Cat# 11930; RRID: AB_2687618
Rabbit anti-IKKβ	Cell Signaling Technology	Cat# 8943; RRID: AB_11024092
Rabbit anti-Phospho-IKKα/β	Cell Signaling Technology	Cat# 2697; RRID: AB_2079382
Mouse anti-IκBα	Cell Signaling Technology	Cat# 4814; RRID: AB_390781
Rabbit anti-Phospho-IκB-α	Cell Signaling Technology	Cat# 2859; RRID: AB_561111
Anti-rabbit IgG, HRP-linked Antibody	Cell Signaling Technology	Cat# 7074; RRID: AB_2099233
Anti-mouse IgG, HRP-linked Antibody	Cell Signaling Technology	Cat# 7076; RRID: AB_330924
Rabbit Anti-RNA polymerase II Antibody	Abcam	Cat# ab264350
Bacterial and virus strains		
IRP1 Lentivirus	GeneChem	N/A
NFKB2 Lentivirus	GeneChem	N/A
Chemicals, peptides, and recombinant proteins		
DMEM/F12, 1:1	Gibco	Cat# 11330500BT
DMEM	Gibco	Cat# 11995500BT
Bovine serum albumin	Sigma-Aldrich	Cat# V900933; CAS: 9048-46-8
Difco Skim Milk	BD biosciences	Cat# BD-232100
polyvinylidene fluoride membrane (0.45μm)	Sigma-Aldrich	Cat# IPVH00010; CAS: 24937-79-9
fetal bovine serum (FBS)	Gibco	Cat# 10270-106
DAPI	Cell Signaling Technology	Cat# 4083
Phalloidin	Cell Signaling Technology	Cat# 13054
DMSO	Sigma-Aldrich	Cat# D2650; CAS: 67-68-5
TMZ	Sigma-Aldrich	Cat# T2577; CAS: 85622-93-1
ECL detection system	Sigma-Aldrich	Cat# WBKLS0500
TRIzol reagent	Thermo Fisher	Cat# 15596026
CCK-8 assay	Dojindo	Cat# CK04
Triton X-100	Sigma-Aldrich	Cat# X100; CAS: 9036-19-5
Phen Green SK	Thermo Fisher	Cat# P14313
IVISbrite D-Luciferin Potassium Salt Bioluminescent Substrate	PerkinElmer	Cat# 122799

(*Continued on next page*)

Continued

REAGENT or RESOURCE	SOURCE	IDENTIFIER
Critical commercial assays		
Whole Cell Lysis Assay	KeyGEN BioTECH	KGP2100
bicinchoninic acid (BCA) assay kit	Beyotime	P0012
PrimeScript™ RT Master Mix	TAKARA	RR036A
TB GREEN Premix Ex Taq	TAKARA	RR420A
Lipid Peroxidation MDA Assay Kit	Beyotime	S0131
GSH and GSSG Assay Kit	Beyotime	S0053
Iron Assay Kit	Sigma-Aldrich	MAK025
JC-1 Assay Kit	Beyotime	C2006
TMRE Assay Kit	Cell Signaling Technology	Cat# 13296
MitoSOX Red fluorescence assay	Thermo Fisher	M36008
ROS Detection Kit	KeyGEN BioTECH	KGT010-1
EZ-Magna ChIP Assay Kit	Sigma-Aldrich	17-10086
Deposited data		
Raw and analyzed data	TCGA	https://cancergenome.nih.gov
RNA-seq data	This paper	GSA-Human: HRA004814
Experimental models: Cell lines		
NHA	Tianjin Medical University General Hospital	N/A
U87	Cell bank of Chinese Academy of Sciences	TCHu138
U251	Cell bank of Chinese Academy of Sciences	TCHu58
LN229	Cell bank of Chinese Academy of Sciences	TCHu244
A172	Cell bank of Chinese Academy of Sciences	TCHu171
U118	Cell bank of Chinese Academy of Sciences	TCHu216
T98	Tianjin Medical University General Hospital	N/A
N9	Tianjin Medical University General Hospital	N/A
N33	Tianjin Medical University General Hospital	N/A
U87TR	Guo Laboratory[38]	N/A
U251TR	Guo Laboratory[38]	N/A
Experimental models: Organisms/strains		
Mouse: BALB/c nude	Southern Medical University	N/A
Oligonucleotides		
Primers for qRT-PCR, see Table S2	This paper	N/A
Primers for ChIP, see Table S3	This paper	N/A
CRISPR sgRNA targeting sequence: IRP1 #1: ATG ACA CGA GCA GGC TTA AA	GeneChem	N/A
CRISPR sgRNA targeting sequence: IRP1 #2: AGA AGA ACT CTG ATC GAA AA	GeneChem	N/A
CRISPR sgRNA targeting sequence: IRP1 #3: TGA TCT ATT ACA AGA TCA GC	GeneChem	N/A
shRNA targeting sequence: NFKB2 #1: GCT GCT AAA TGC TGC TCA GAA	GeneChem	N/A
shRNA targeting sequence: NFKB2 #2: CCT GTA ACA GTG TTT CTG CAA	GeneChem	N/A
shRNA targeting sequence: NFKB2 #3: GCC CAA TTT AAC AAC CTG GGT	GeneChem	N/A

(*Continued on next page*)

Continued

REAGENT or RESOURCE	SOURCE	IDENTIFIER
Software and algorithms		
ImageJ	NIH	https://imagej.nih.gov/ij/
GEPIA 2	Zhang's Lab	http://gepia2.cancer-pku.cn
FlowJo v10.8.1	BD Biosciences	https://www.flowjo.com/
Living Image 4.5.2	Caliper LifeScience	https://www.perkinelmer.com.cn/
GraphPad Prism 8	GraphPad	https://www.graphpad.com/
NIS-Elements	Nikon	https://www.microscope.healthcare.nikon.com/
Leica Application Suite X	Leica	https://www.leica-microsystems.com.cn/

RESOURCE AVAILABILITY

Lead contact

Requests for further information should be directed to Hongbo Guo (guohongbo911@126.com).

Materials availability

This study did not generate new unique reagents.

Data and code availability

The raw sequence data reported in this paper have been deposited in the Genome Sequence Archive in National Genomics Data Center, China National Center for Bioinformation/Beijing Institute of Genomics, Chinese Academy of Sciences (GSA-Human: HRA004814) that are publicly accessible at https://ngdc.cncb.ac.cn/gsa-human.

This paper does not report original code.

Any additional information required to reanalyze the data reported in this paper is available from the lead contact upon request.

EXPERIMENTAL MODEL AND STUDY PARTICIPANT DETAILS

Cell culture

Patient-derived GBM cells (N9 and N33), NHA and T98 acquired from Tianjin Medical University General Hospital were cultured in Dulbecco's Modified Eagle's Medium (DMEM/F12, 1:1; Gibco, C11330500BT) supplemented with 1% Penicillin-Streptomycin and 10% fetal bovine serum (FBS, Gibco, 10270-106). The human cell lines U87, U251, LN229, A172 and U118 were purchased from Cell bank of Chinese Academy of Sciences (Shanghai, China), and it was authenticated and tested for mycoplasma contamination. The TMZ-resistant lines, U87TR and U251TR, were established and maintained in our laboratory.[38] The cells were routinely cultured in DMEM (Gibco, C11995500BT) containing 1% Penicillin-Streptomycin and 10% FBS. To maintain the TMZ-resistant phenotype, U87TR and U251TR were alternately cultured in TMZ-free medium and medium containing TMZ (200 μg/mL). TMZ was obtained from Sigma-Aldrich (T2577, San Francisco, CA, USA) and dissolved in dimethyl sulfoxide (DMSO, Sigma-Aldrich, D2650, USA) at a final concentration of 50 μg/mL. All the cells were incubated at 37°C in 5% CO_2.

In vivo anti-tumor activity

Four-to five-week-old female BALB/c nude mice were obtained from the Laboratory Animal Center, Southern Medical University. To study the role of IRP1 in TMZ resistance, the mice were randomly divided into four groups (n = 6 per group) (U87TR, U87TR+TMZ, U87TR-lvIRP1, U87TR-lvIRP1+TMZ). To establish the GBM models, IRP1 overexpress or control U87TR cells (5×10^5 cells per mice in 3 μL PBS) transfected with luciferase lentivirus were injected into the mice brain under the guidance of a stereotactic instrument at coordinates relative to bregma: 2.0 mm posterior, 2.0 mm lateral, and 3.0 mm ventral. For TMZ treatment groups, mice injected cells for 14 days were treated with TMZ (at a dose of 5 mg/kg) at the frequency of 5 days on and 2 days off for 2 weeks. Bodyweights were monitored regularly. In addition, survival of mice was monitored during the tumor progression and overall survival curves were generated using the

Kaplan–Meier method. Bioluminescence imaging was performed to detect intracranial tumor growth on days 7, 14, 21 and 28 by the IVIS Spectrum imaging system. On day 28, the mice were sacrificed, and their brain tissues were excised, fixed in 4% PFA, and embedded in paraffin for Hematoxylin and Eosin (H&E) and immunohistochemical (IHC) staining. All animal work was approved by the Animal Experiment Ethics Committee of Zhujiang Hospital in accordance with the Institutional Animal Care and Use Committee Guidelines (approval number LAEC-2021-162).

METHOD DETAILS

CRISPR/Cas9 system and sequencing

The CRISPR/Cas9 gene-editing system (GeneChem, Shanghai, China) was used to generate the LV-Cas9-sgRNA-IRP1 stable cell lines. Lentiviral vectors (LVs) harbouring Cas9 and sgRNA were constructed for transfection of the U87 and U251 cells. According to the manufacturer's protocol, the LVs harbouring Cas9 were transfected into the cells using polybrene (GeneChem, Shanghai, China) to isolate the stable cell lines. In addition, three different sgRNAs were designed according to the three different target sites in the IRP1 gene and packaged into the LVs to form LV-sgRNA-IRP1. Sequencing was performed using the Sanger method (GeneChem, Shanghai, China) to confirm the sequence of the three sgRNAs. The sequences of the sgRNAs were as follows: #1 ATG ACA CGA GCA GGC TTA AA; #2 AGA AGA ACT CTG ATC GAA AA; and #3 TGA TCT ATT ACA AGA TCA GC. The three LV-sgRNA-IRP1s were transfected into the U87 and U251 cells to eventually generate the LV-Cas9-sgRNA-IRP1 stable cell lines, and 48 h following LV transfection, subsequent experiments were performed.

Cell transfection

IRP1 and NFKB2 lentiviral vectors were transduced to U87TR, U251TR and U87, U251 according to the manufacturer's instructions (GeneChem, Shanghai, China) to generate stable overexpression cells. Short Hairpin RNAs (shRNAs) targeting NFKB2 was synthesized by GeneChem (Shanghai, China). Sequences of shRNAs were as follows: #1 GCT GCT AAA TGC TGC TCA GAA; #2 CCT GTA ACA GTG TTT CTG CAA; #3 GCC CAA TTT AAC AAC CTG GGT. The positive transfected cells were selected by puromycin for two weeks at 2.5 μg/mL. The transfection efficiency was confirmed by Western Blot and qRT-PCR.

Western Blot analysis

Proteins were extracted from cells with Whole Cell Lysis Assay (KeyGEN BioTECH, KGP2100, Jiangsu, China) on ice and quantified with bicinchoninic acid (BCA) assay kit (Beyotime, P0012, Beijing, China). Protein lysates were separated by SDS-polyacrylamide gel electrophoresis and then transferred onto polyvinylidene fluoride (PVDF) membranes (Millipore, IPVH00010, USA). The membranes were incubated with primary antibodies overnight, followed by incubation with horseradish peroxidase (HRP)-conjugated secondary antibodies (Cell Signaling Technology, MA, USA) for 1 h. Immunoreacted bands were visualized via ImageQuant LAS500 chemiluminescence (General Electric, Boston, USA) through ECL detection system (Millipore, WBKLS0500, USA). Finally, the protein expression was analyzed by the software of ImageJ (National institution of Health, USA), and β-actin was used as loading control. The primary antibodies were listed in Table S1.

RNA extraction and quantitative RT-PCR

TRIzol reagent (Invitrogen, 15596026, USA) was used to extract the total RNA from cultured cells, and cDNA was synthesized using PrimeScript RT Master Mix (Takara Bio, RR036A, Shiga, Japan) according to manufacturer's instructions. Quantitative real-time PCR was performed using TB GREEN Premix Ex Taq (Takara Bio, RR420A, Shiga, Japan) on an ABI StepOne Plus real-time instrument (Thermo Fisher Scientific, Waltham, MA) and the results were normalized to the GAPDH. ΔΔCt method was used for quantification analysis with at least 3 independent experiments. The prime sequences were listed in Table S2.

Cell viability assay

Cells (5×10^3 per well) were seeded into 96-well plates and cultured for 24 h. The media was then replaced with fresh media containing different formulations. The viability of treated cells was determined using the CCK-8 assay (Dojindo, CK04, Kumamoto, Japan) following the manufacturer's instructions after incubation at 37°C for 2 h. The values of optical density (OD) 450 nm were detected using a microplate reader (BioTek, Winooski, VT).

Immunofluorescence and confocal imaging

Cells cultured and fixed on confocal dishes were fixed with 4% paraformaldehyde and permeabilized with 0.5% Triton X-100 (Sigma-Aldrich, X100, USA) in PBS for 15 min followed by blocking with 5% bovine serum albumin (BSA). The primary antibodies were incubated overnight at 4°C followed by corresponding secondary antibody incubation for 1 h at room temperature. Nuclear counterstaining was conducted with DAPI (Cell Signaling Technology, #4083, USA). Cells were stained with phalloidin (dilution 1:200; Cell Signaling Technology, #13054, USA) to highlight actin. Confocal images of the cells were captured using laser confocal microscope (Nikon, Japan).

Measurement of MDA

Malondialdehyde (MDA) levels in cells and tumors were measured using Lipid Peroxidation MDA Assay Kit (Beyotime, S0131, China) in accordance with the manufacturer's instructions. In brief, cells or tumors were homogenized and centrifuged to separate the supernatant. Thiobarbituric Acid (TBA) solution was then added to the supernatant and reacted in an acidic and high-temperature environment for 15 min. After the reaction, the supernatant was obtained by centrifugation, and the absorbance was evaluated at 532 nm using a microplate reader (BioTek, Winooski, VT).

Measurement of GSH/GSSG

The intracellular concentration of total reduced glutathione (GSH) and oxidized glutathione disulfide (GSSG) was measured using a GSH and GSSG Assay Kit (Beyotime, S0053, China) according to the manufacturer's protocol. A standard curve could be plotted according to the determination of A412 with microplate reader (BioTek, Winooski, VT). Then, use the specific formula to calculated reduced GSH concentration.

Transmission electron microscopy (TEM)

For TEM, cells were fixed with 2.5% glutaraldehyde, followed by 1% osmium tetroxide treatment for 1–2 h, and dehydration in graded ethanol, finally embedding the samples in epoxy resin. 100 nm ultra-thin slices were sectioned, stained with 2% uranyl acetate and lead citrate, and finally imaged with the Tecnai G2 Spirit microscope.

Iron assay

According to the Iron Assay Kit (Sigma Aldrich, MAK025, USA), cells were added to iron assay buffer on ice and centrifuged at 16,000 g for 10 min at 4°C to obtain the supernatant. 50 μL of the supernatant was incubated with 50 μL of assay buffer in a 96 multi-well microplate for 30 min at 25°C. Samples were incubated with 100 μL of the iron probe for 60 min at 25°C while protected from light. The absorbance at 593 nm was measured using a microplate reader (BioTek, Winooski, VT). The final iron concentration was calculated by the corresponding formula. The chelatable intracellular iron pool was determined by using the fluorescent probe Phen Green SK (Invitrogen, P14313, USA). Cells were cultured on confocal dishes and loaded with 20 μM Phen green SK for 30 min in PBS. The cells were then washed with PBS and imaged using a laser confocal microscope (Leica, Germany). The experiments were performed in triplicate.

Mitochondrial membrane potential assay

Mitochondrial membrane potential was detected using the JC-1 Assay Kit (Beyotime, C2006, China) and the TMRE Assay Kit (Cell Signaling Technology, #13296, MA, USA). According to the manufacturer's protocols, Cells fixed on confocal dishes were stained with JC-1 working solution and TMRE Labeling Solution respectively for 20 min at 37°C in an incubator and analyzed using laser confocal microscope (Leica, Germany). Assays were performed in triplicate, and fluorescence intensities were calculated using ImageJ software.

Mitochondrial and intracellular reactive oxygen species

Mitochondrial ROS levels were measured by the MitoSOX Red fluorescence assay (Life Technologies, M36008, USA). Cells were incubated in 5 μM MitoSOX reagent in PBS containing 5% FBS at 37°C for 10 min, protected from light and analyzed using a laser confocal microscopy (Nikon, Japan). Intracellular ROS were measured by a ROS Detection Kit (KeyGEN BioTECH, KGT010-1, Jiangsu, China). According to the protocol, a serum-free culture solution was used to prepare a DCFH-DA solution with a final concentration of 10 μM. The cells collected were suspended in the DCFH-DA solution and incubated at 37°C for

20 min. The solution was mixed by inversion every 3–5 min so that the probe would fully contact the cells. The cells were washed three times with serum-free cell culture medium to fully remove the DCFH-DA, which did not enter the cells. The ROS levels were analyzed using flow cytometry (Sony, Japan) and laser confocal microscope (Leica, Germany), respectively.

RNA-seq analysis

Total RNA was extracted from U87-IRP1-NC and U87-IRP1-KO using TRIzol Reagent (Invitrogen, 15596026, USA) following the manufacturer's instructions and assessed for the RIN number to inspect RNA integrity by an Agilent 4200 TapeStation. Sequencing libraries were generated following the manufacturer's recommendations, and index codes were added to attribute sequences to each sample. RNA was sequenced by HaploX (Jiangxi, China) on the Illumina PE150 platform. Paired-end clean reads were aligned to the human genome hg19 using HISA T2 v2.1.0, which is a highly efficient system for aligning reads from RNA sequencing experiments. Differential expression analysis of two groups was performed using the DESeq R package (1.18.1). Unsupervised clustering was performed using cluster and tree views and visualized using heat maps. KEGG enrichment analysis and visualization of differentially expressed genes was implemented by the clusterProfiler R package, which is a simple-to-use tool to analyze high-throughput data obtained from transcriptomics or proteomics. Genes with adjusted p value less than 0.05 were considered significantly enriched by differential expressed genes.

Chromatin immunoprecipitation (ChIP) assay

ChIP assay was executed using the EZ-Magna ChIP Assay Kit (Millipore, 17-10086). Briefly, 2×10^7 U87 cells were cross-linked with 1% formaldehyde for 10 min at room temperature, and neutralized with 10× glycine for 5 min at room temperature. Subsequently, samples were sonicated in lysis buffer to obtain 200-1,000 bp DNA fragments and the extraction of ChIP DNA was performed as per the kit's protocol. And we used the antibody NF-κB2 (Cell Signaling Technology, 1:50 dilution). The primer sequences specific to the promoter region of LCN2 and FPN1 are listed in Table S3.

H&E and immunohistochemical staining

Sections (4-5μm) were cut from paraffin-embedded tissue samples, dewaxed, and hydrated, and antigen retrieval was performed in citrate at 95°C for 30 min. Sections were incubated with primary antibody against Ki67 (ZSGB-BIO, ZM-0167, dilution 1: 100) at 4°C overnight and subsequently HRP-conjugated secondary antibody for 1 h at room temperature. Visualization was performed using the substrate Diaminobenzidine (DAB), and sections were stained with hematoxylin and eosin. Digital images were acquired under a scanner (3DHISTECH, Hungary). Quantitative analysis was evaluated by Image J.

QUANTIFICATION AND STATISTICAL ANALYSIS

Statistical analysis and graphing were performed using GraphPad Prism 8 (GraphPad Software, San Diego, CA, USA). All data were presented by mean ± standard deviation (SD). The Student's t-test was used to compare experimental groups and control groups. For multiple experimental groups, one-way or two-way ANOVA was used. Levene statistic was used to evaluate the variance homogeneity of the data. Kaplan–Meier survival curves were compared using the log-rank test to assess survival differences between groups. All the experiments were repeated at least three times with triplicates unless stated otherwise. Significance was defined as *$p < 0.05$, **$p < 0.01$, ***$p < 0.001$, ****$p < 0.0001$, #$p < 0.05$, ##$p < 0.01$, ###$p < 0.001$, ####$p < 0.0001$, ns = not significant.